Widespread occurrences of variably crystalline ^{13}C-depleted graphitic carbon in banded iron formations

Matthew S. Dodd[1,2,3], Dominic Papineau[1,2,3,4], Zhen-Bing She[4], Chakravadhanula Manikyamba[5], Yusheng Wan[6], Jonathan O'Neil[7], Juha Karhu[8], Hanika Rizo[9], Franco Pirajno[10]

[1] *London Centre for Nanotechnology, University College London WC1H 0AH UK*
[2] *Department of Earth Sciences, University College London WC1E 6BT UK*
[3] *Centre for Planetary Sciences, University College London, WC1E 6BT UK*

[4] *School of Earth Sciences & State Key Laboratory of Biogeology and Environmental Geology, China University of Geosciences, Wuhan, China*

[5] *National Geophysical Research Institute, Hyderabad, India*

[6] *Beijing SHRIMP Centre, Institute of Geology, Chinese Academy of Geological Sciences, China*
[7] *Department of Earth and Environmental Sciences, University of Ottawa, Ottawa, K1N 6N5 Canada*
[8] *Department of Geosciences and Geography, University of Helsinki, P.O.Box 64 Finland*
[9] *Department of Earth Sciences, Carleton University, Ottawa, ON K1S 5B6, Canada*
[10] *Centre for Exploration Targeting, The University of Western Australia, 35 Stirling Highway, Crawley, WA 6009 Australia*

Abstract

Almost all evidence for the oldest traces of life on Earth rely on particles of graphitic carbon preserved in rocks of sedimentary protolith. Yet, the source of carbon in such ancient graphite is debated, as it could possibly be non-biological and/or non-indigenous in origin. Here we describe the co-occurrence of poorly crystalline and crystalline varieties of graphitic carbon with apatite in ten different and variably metamorphosed banded iron formations (BIF) ranging in age from 1,800 to >3,800 Myr. In Neoarchean to Palaeoproterozoic BIF subjected to low-grade metamorphism, ^{13}C-depleted graphitic carbon occurs as inclusions in apatite, and carbonate and arguably represents the remineralisation of syngenetic biomass. In BIF subjected to high-grade metamorphism, ^{13}C-depleted graphite co-occurs with poorly crystalline graphite (PCG), as well as apatite, carbonate, pyrite, amphibole and greenalite. Retrograde minerals such as greenalite, and

veins cross-cutting magnetite layers contain PCG. Crystalline graphite can occur with apatite and orthopyroxene, and sometimes it has PCG coatings. Crystalline graphite is interpreted to represent the metamorphosed product of syngenetic organic carbon deposited in BIF, while poorly crystalline graphite was precipitated from C-O-H fluids partially sourced from the syngenetic carbon, along with fluid-deposited apatite and carbonate. The isotopic signature of the graphitic carbon and the distribution of fluid-deposited graphite in highly metamorphosed BIF is consistent with carbon in the fluids being derived from the thermal cracking of syngenetic biomass deposited in BIF, but, extraneous sources of carbon cannot be ruled out as a source for PCG. The results here show that apatite + graphite is a common mineral assemblage in metamorphosed BIF. The mode of formation of this assemblage is, however, variable, which has important implications for the timing of life's emergence on Earth.

Key words: early life; banded iron formation; carbon isotopes; Raman; graphite; biosignatures

1.0 Introduction

The association of isotopically-light organic carbon and apatite is a common feature of sediments incorporating biomass (Papineau et al., 2016; She et al., 2014). Apatite [$Ca_5(PO_4)_3$(F, Cl, OH)] requires phosphorus, which can be derived from the decomposition of phosphorus-bearing biological organic matter (biomass) in sediments. This knowledge has been combined with observations of isotopically-light carbon in graphite in association with apatite, to argue for a biological origin of graphite (Mojzsis et al., 1996) in the ca. 3,830 million years old (Myr) Akilia quartz-pyroxene rock. Additionally, the presence of apatite rosettes (Li et al., 2012) and apatite with ferric acetate (Li et al., 2011) have been used to propose the biological processing of phosphorus and organic carbon in BIF. Alternatively, it has been suggested that graphite associated with apatite in metamorphosed BIF may also be fluid-deposited (Lepland et al., 2011; Papineau et al., 2010a; Papineau et al., 2011; Papineau et al., 2010b), so that non-biological and biological sources of organic carbon are both possible. To assess how common associations of graphitic carbon and apatite are in BIF, as well as the origin of the carbon in graphite, we document its mineral associations in ten different samples of various ages and metamorphic grades. Selected samples come from the Eoarchaean supracrustal terranes of Nuvvuagittuq, Akilia, and Saglek, from the Neoarchean belts of Sandur, Temagami, Anshan, and Wutai, as well as from the Paleoproterozoic Brockman, Pääkkö, and Biwabik iron formations (Table 1; Figure 1; Supplementary information).

2.0 Methods

2.1 Optical microscopy

Standard 30 μm thick, polished and doubly-polished thin sections were prepared with a final polishing step using Al_2O_3 0.5μm powder for investigation using transmitted and reflected light microscopy. No immersion oil was used to map petrographic features in thin section.

2.2 Micro-Raman spectroscopy

Micro-Raman microscopy was conducted on petrographic targets within the polished thin sections using a WiTec alpha300 confocal Raman imaging microscope with a 532nm wavelength laser and operating at a power between 0.1 and 6mW depending on the target. Raman spectra and hyperspectral scans were performed at 100X magnification with variable spatial resolutions from 1μm to 360nm, and spectral resolutions of $4cm^{-1}$ were achieved using a 600 lines/mm grating. Hyperspectral images were created for specific mineral phases using peak intensity mapping for characteristic peaks of each individual mineral in a scan. Average spectra were calculated by creating a mask on homogeneous pixels of individual phases and had their backgrounds fitted to a polynomial function and subtracted. Large area scans (>100µmx100µm) were completed using the same process outlined previously, with spatial resolutions no lower than 1µm. Peak parameters were calculated from a Lorenz function modelled for each selected peak. Cosmic ray reduction was applied to all Raman spectra. Raman spectra were collected at confocal depths of at least 1µm below the surface of the thin sections. Raman spectrum parameters, such as peak positions, Full Width at Half Maximum (FWHM), and areas under the curve were extracted from the best-resolved Raman peaks, and modelled with Lorentz function on background-subtracted spectra. To estimate maximum crystallisation temperatures of graphitic carbon from the Raman spectra, we used the geothermometer of Beyssac et al. (2002), which is justified by the lower greenschist to granulite metamorphic grade of all the studied banded iron formations.

2.3 Scanning electron and energy dispersive x-ray spectroscopy

Scanning electron microscopy (SEM) in back scattered electron (BSE) and secondary electron (SE) imaging modes were used to characterise the morphology and composition of selected targets, which were also characterised by energy dispersive x-ray spectroscopy (EDS). Analyses were carried out in the Department of Earth Sciences at University College London (UCL) using a JEOL JSM-6480L SEM. Standard operating conditions for SEM imaging and EDS analysis were a 15kV accelerating voltage, working distance of 10mm and an electron beam current of 1nA. Samples were always coated with a few nanometres of Au prior to analysis.

The analyses were calibrated against standards of natural silicates, oxides and Specpure® metals, with the data corrected using a ZAF program.

2.4 Stable isotope mass spectrometry

Analyses of bulk rock powders for graphitic carbon were conducted in the Bloomsbury Environmental Isotope Facility at UCL with a Thermo-Finnigan Flash 1112 EA connected to a Thermo Delta V Isotope Ratio Mass Spectrometer via a Conflo IV gas distribution system. Sample preparation and analytical details follow a previously devised protocol (Dodd et al., 2018). A suite of standard materials that span a range of $\delta^{13}C$ values from -26‰ to -6‰, was analysed within each run. Each standard was analysed multiple times through the run to ensure reproducibility. The results were calibrated to the Vienna Pee Dee Belemnite (VPDB) scale with a reproducibility better than 0.2‰ (1σ; n=19). Empty muffled silver capsules were ran with and without HCl added to test for contamination prior to analysis. No carbon was detected in these procedural blank silver capsules. Analyses of bulk rock powders for carbonate were conducted in the Cardiff School of Earth Sciences with a Thermo Finnigan Delta V Advantage mass spectrometer connected to a Gas Bench II. Sample preparation and analytical details follow a previously devised protocol (Dodd et al., 2018).

3.0 Results and discussion

3.1 Occurrences of graphitic carbon in highly metamorphosed BIF

Apatite in the amphibolite facies ca. 4,280-3,770 Myr Nuvvuagittuq silicate BIF (quartz+magnetite+Fe-silicates; Table 1; Fig. 1) appears with fluid inclusions of CO_2+CH_4+H_2O (Fig. 2) within quartz grains, along grain boundaries and with retrograde greenalite (Fig. 3a; Supplementary Table 1). In the Nuvvuagittuq jasper BIF (quartz+haematite+magnetite), apatite occurs as inclusions in calcite rosettes, chert+magnetite granules, and as millimetre-size graphite-bearing euhedral laths (Dodd et al., 2017). Notably for the Nuvvuagittuq silicate BIF, graphite co-occurs with poorly crystalline graphite (PCG) as coatings on apatite, which also hosts inclusions of magnetite, calcite and graphite (Fig. 3a-d). Poorly crystalline graphite has more intense Raman D peaks than G peaks, which yields D/ G peak intensity ratios above 1, in contrast to crystalline graphite which has weak intensity D peaks compared to G peaks, giving intensity ratios below 1 (Fig. 4; Supplementary Fig. 1). These differences lead to estimates of crystallisation temperatures for PCG between 60-200°C lower than those of graphite in the same sample (Fig. 4; Supplementary Table 2). In the Nuvvuagittuq silicate BIF, PCG appears within phyllosilicate masses of greenalite and minnesotaite, and occurs with accessory minerals such as carbonate and sulphide that are present in between coarse quartz crystals (Fig. 3e-g), which demonstrates a retrograde origin. Furthermore, PCG occurs within orthopyroxene crystals and coats calcite and retrograde hornblende inclusions (Fig. 3h-j; Supplementary Table 1). In other instances, PCG and graphite co-exist with calcite and magnetite inside orthopyroxene crystals (Fig. 5). Similarly, in the ca. 3,920 Myr old Saglek-Hebron silicate BIF (Table 1; Fig. 1), crystalline graphite appears inside apatite and as coatings on apatite (Fig. 3j-l), demonstrating that this is a common mineral association among Eoarchean BIF.

The ca. 2,551 Myr old, amphibolite facies Anshan BIF (Table 1; Fig. 1), also hosts inclusions of PCG associated with greenalite and apatite along with graphite. Graphite is also present within prograde grunerite crystals (Fig. 6a-b). Similarly, both graphite and PCG have been found in association with apatite and greenalite in carbonate, situated adjacent to magnetite-pyrite bands (Fig. 6c-d). In the ca. 2,500 Myr, greenschist facies Wutai BIF (Table 1; Fig. 1), apatite forms microscopic clusters within masses of ankerite present in pyrite-rich layers, in which graphite co-occurs within microns of PCG, apatite and feldspar (Fig. 6e-f). In the ca. 1,878 Myr hornfels-pyroxene facies Biwabik BIF (Table 1; Fig. 1), graphite occurs with calcite within retrograde grunerite, as evidenced by grunerite appearing as rims along the margins of orthopyroxene (Fig. 6g-h). Similarly in the ca. 3,830 Myr old granulite facies Akilia quartz-pyroxene rock (Table 1; Fig. 1), graphite also occurs within retrograde grunerite rims along the margins of orthopyroxene crystals, occasionally associated with chalcopyrite (Papineau et al., 2010a) (Supplementary Figure 2). In contrast, abundant graphite is found in discrete layers of prograde grunerite, pyrite, feldspar, and magnetite with apatite (Fig. 6h-j) in the ca. 2,000 Myr old, lower amphibolite facies Pääkkö BIF (Table 1; Fig. 1).

3.2 Occurrences of graphitic carbon in BIF metamorphosed to the greenschist facies

Graphitic carbon was also mapped by micro-Raman in the greenschist facies Dales Gorge, Temagami and Sandur BIF (Table 1; Fig. 1). In the ca. 2,470 Myr Dales Gorge BIF (Table 1; Fig. 1), apatite can form variably thick bands varying up to 600µm in thickness. These bands are associated with stilpnomelane or minnesotaite and siderite/ ankerite between magnetite layers. The apatite contains numerous inclusions of microscopic haematite, ankerite, graphitic carbon and pyrite (Fig. 7a-b). The graphitic carbon tends to form discrete layers in the apatite and cluster around ankerite inclusions within the apatite (Fig. 7b). Graphitic carbon is preferentially preserved within the apatite, with minor amounts in the surrounding quartz and ankerite (Fig. 7b). In the ca. 2,736 Myr Temagami BIF (Table 1; Fig. 1), there are magnetite and minnesotaite bands interlayered with apatite bands, which are nearly one millimetre thick, with inclusions of ankerite and graphitic carbon (Fig. 7c-d). In contrast to the Dales Gorge BIF, the Temagami graphitic carbon occurs predominately in ankerite inclusions within millimetre thick apatite bands (Fig. 7d). The ca.

2,700 Myr Sandur BIF (Table 1; Fig. 1) preserves a range of graphitic carbon crystallinities (Fig. 7e-g; 4) including graphite and PCG, which occur with apatite, siderite and pyrite. Hence, these observations show for the first time that graphite and PCG co-occur in BIF, and that they are also commonly associated with apatite and carbonate.

3.3 Syngenicity of graphitic carbon

Graphitic carbon may be damaged during polishing of petrographic thin sections, but can be distinguished by enlarged D peaks in the Raman spectra (Beyssac et al., 2003). Therefore, it has been verified through optical microscopy that all PCG targets are found below the thin section surface and were not modified by polishing. In addition, orientation of graphite sheets relative to the Raman laser may induce changes in the relative intensities of the D peak (Wang et al., 1989). Yet, graphite sheet orientation creates relatively minor changes in D peak intensities and could not account for the large difference in intensities of D to G peaks observed here between PCG and graphite (Supplementary Fig. 1 and Supplementary Table 2). The crystalline structural differences between PCG and graphite are therefore a result of their mode of formation, and the two types can be clearly distinguished by Raman crystallographic characteristics (Supplementary Fig. 1).

The crystallisation temperature estimates for PCG are interpreted as retrograde crystallization temperatures of fluid-deposited graphite, although we stress these may not be accurate, as the graphite-Raman thermometer was calibrated against prograde mineral assemblages (Beyssac et al., 2002) (Supplementary Table 2). A better judge of precipitation temperatures can be discerned from the occurrence of PCG with retrograde minerals like minnesotaite (Fig. 3f-I; 6a-d, g), which has an upper stability limit of 350°C (Klein, 2005), similar to the crystallisation temperatures calculated for PCG (Supplementary Table 2). This indicates that PCG was deposited from low temperature fluids during retrograde metamorphism in the Nuvvuagittuq, Anshan and Wutai BIF, supported by PCG appearing within veins cross-cutting sedimentary layers in the Nuvvuagittuq BIF (Fig. 1). However, retrograde minerals hosting graphitic carbon have not yet been found in the Wutai BIF. In the case of the granulite facies Biwabik BIF and Akilia quartz-pyroxene rock, graphite is associated with retrograde grunerite rims on prograde orthopyroxene crystals (Fig. 6g; Supplementary Fig. 2), depicting high temperature retrogression with carbonic fluids. However, the Dales Gorge, Temagami and Pääkkö BIF do not show evidence for retrogression, and preserve primary organo-mineral assemblages, indicative of metamorphosed, decayed biomass, such as ^{13}C-depleted kerogen inclusions in apatite and ^{13}C-depleted carbonate (Fig. 7a-d; Table 2). Crystallisation temperature estimates for graphite in the Sandur BIF exceeds metamorphic temperatures experienced by the formation (Supplementary Table 2), and therefore may be a result of non-metamorphic processes, such as templated mineral growth along quartz boundaries (Fig. 7g)(van Zuilen et al., 2012).

The retrograde phases in the Nuvvuagittuq, Anshan, Biwabik and Akilia are hydrated phyllosilicates and double-chained inosilicates (Fig. 3g-j; 6d, g-h, Supplementary Fig. 2). This points to cooling and hydration reactions as the precipitation mechanism of PCG (Luque et al., 2014). This can happen during cooling of C-O-H fluids and can lead to coinciding hydration of the host minerals and decreased carbon solubility, so that PCG precipitates (cf. Equ. 1). In amphibolite facies BIF, amphiboles such as grunerite are prograde minerals, whereas in granulite facies BIF grunerite rims on pyroxene are more likely retrograde after pyroxene (Klein, 2005). Greenalite and minnesotaite would not survive amphibolite facies metamorphism and therefore they are also retrograde minerals (Klein, 2005).

$$CO_2 + CH_4 \rightarrow 2C + 2H_2O \qquad \text{Equation 1}$$

Significantly, the association of apatite with fluid inclusion trails in the Nuvvuagittuq BIF (Fig. 2) shows that fluids contained CO_2, CH_4, H_2O, H_2S, PO_4^{3-}, Ca^{2+}, Fe^{2+} and Cu^{2+} (Papineau et al., 2011), as indicated by the occurrence of chalcopyrite, calcite, apatite, and Fe^{2+}-bearing silicates along with fluid inclusions (Fig. 1). In the Akilia quartz-pyroxene rock, metamorphic apatite has been reported to contain carbonate, which could have been a source of carbon in graphite (Nutman and Friend, 2006). Graphite coatings on apatite in the Akilia quartz-pyroxene rock (Papineau et al., 2010a) co-occur in fluid inclusion trails containing CO_2+CH_4+H_2O (Lepland et al., 2011), as well as sulphides and carbonate (Supplementary Fig. 2), which point to fluid-deposition from fluids compositionally-similar to those in the Nuvvuagittuq BIF. An important observation in the Nuvvuagittuq BIF, is that minnesotaite and greenalite are the dominant phyllosilicate minerals associated with PCG, which suggests that the metamorphic fluids were largely derived from within the BIF because these phases are common in BIF. Should the metamorphic fluids have been sourced from non-BIF lithologies, they would carry elevated concentrations of elements atypical for BIF, such as Ti or Al. Thus the absence of mica with PCG is consistent with the fluids being derived mainly from BIF elements (Fig. 3f-g) (Gaillard et al., 2018). The association of PCG and apatite can be explained by hydroxyapatite and phyllosilicates co-precipitating from fluids. These minerals would consume H_2O during precipitation reactions yielding PCG and H_2O through Equation 1. This precipitation of apatite is analogous to the dissolution and recrystallisation of graphite and carbonate-bearing apatite from granulite facies pelitic rocks of Cooma, South-East Australia (Nutman, 2007). Such processes can result in the observed association of apatite and graphitic carbons during retrograde reactions. In general, carbonate appears as microscopic crystals intimately associated with fluid-deposited carbon, probably as a result of increasing CO_2 disassociation in metamorphic fluids during cooling (Fig. 2; 3d, g, I; 6g).

3.4 Origins of poorly crystalline and crystalline graphitic carbon

PCG and graphite co-occur within micrometre distances in the Nuvvuagittuq, Anshan, and Wutai BIF (Fig. 3b-d; 5b-h; 6a-f). From the intimate association of these graphitic carbon phases, it can be inferred that they bear the same source and were transported together by similar metamorphic fluids. This is supported by PCG commonly found around, or coating, crystalline graphite in these BIF (Fig. 3a-d; 5d-h; 6d, f). This implies that the PCG grew on pre-existing crystalline graphite. Similar examples have been found in Proterozoic gneiss and quartzite from the Iberian metamorphic belt of Spain, where fluid-deposited graphite forms overgrowths on syngenetic graphite in gneiss and quartzite (Crespo et al., 2004), as well as in numerous other formations (Arita and Wada, 1990; Satish-Kumar et al., 2011; Valley and O'Neil, 1981). In addition, multiple crystallinities of disordered organic carbon have been found co-occurring in chert from the Apex Formation (Marshall et al., 2012) in Western Australia, and with graphite in greenschist and amphibolite grade pelitic rocks (Kribek et al., 2008; Large et al., 1994). Varying crystallinity of graphitic carbon in metamorphic terranes may be due to the preservation of fluid-deposited graphite along with syngenetic graphite (Crespo et al., 2004), or varying temperature and H_2 fugacity of C-O-H fluids during deposition of graphite (Pasteris and Chou, 1998).

Graphite and PCG in the Nuvvuagittuq, Anshan and Wutai BIF, therefore, have one of two possible mechanisms of formation: 1) the graphite was formed from metamorphism of organic matter deposited in the sedimentary rocks and PCG precipitated from C-O-H fluids

(Crespo et al., 2005), or 2) all graphitic carbon was precipitated from C-O-H fluids, of varying temperature or H_2 fugacity, which precipitated carbon (Pasteris and Chou, 1998) with varying crystallinities. In the Nuvvuagittuq BIF, PCG veins (Fig. 1) contain only PCG, and not graphite, suggesting there was just one generation of fluid-deposited graphite. Additionally, crystalline graphite does not appear with retrograde minerals, which suggests that only PCG was fluid-deposited. Low temperatures are required for PCG precipitation from C-O-H, so that fluid-deposited PCG is relatively uncommon in nature due to the high solubility of carbon at low temperatures (Luque and Rodas, 1999; Pasteris, 1999). The low fO_2 and high CH_4 content of carbonic fluids generated at low pressures and temperatures (French, 1966) from the maturation of organic matter encourage precipitation of disordered graphite, where it would otherwise be unstable in typically more oxidised crustal carbonic fluids (Pasteris, 1999). Low-temperature carbonic fluids are close to graphite saturation and precipitate graphite they move, rather than transporting carbon long distances. This may be due to the low temperature of the fluids, making them susceptible to abrupt changes in pressure-temperature (Pasteris, 1999). Much of this graphite may nucleate on pre-existing graphite, thereby making carbon unavailable for widespread deposition (Crespo et al., 2004; Pasteris, 1999).

The distances of carbon transport in the Nuvvuagittuq appear to have ranged from a few microns to perhaps centimetres, as evidenced by PCG within micron-sized veins cutting across thin sections (Fig. 1). This is in contrast to high temperature graphite deposits, which transfer carbon over long distances in the crust, from 10s of metres to possibly kilometres (Luque et al., 2014). Since there are no reported graphite veins cross-cutting the Nuvvuagittuq belt, graphite was likely not widely mobile. The association of crystalline graphite and PCG, together with the lack of widely distributed graphite veins, (over 10s of metres to kilometres) is consistent with a localised source of carbon. Therefore, PCG in the Nuvvuagittuq, Anshan and Wutai BIF (Fig. 3a-d; 5d-h; 6a-f) was likely partly sourced *in-situ,* and precipitated within centimetres of the source, from low fO_2 and high CH_4 carbonic fluids. The occurrence of PCG on the rims of crystalline graphite in isolated orthopyroxene crystals is unlikely to arise from infiltration of external H_2O+CO_2+CH_4 fluids, without leaving nearby trails of PCG, which are not seen in Raman or optical images (Fig. 5). This observation is consistent with localised H_2O+CO_2+CH_4 fluids being partially sourced *in-situ* from syngenetic organics (now crystalline graphite). Though it is not possible to fully exclude an external source for some of the carbon in the C-O-H fluids, it is concluded that PCG in the Nuvvuagittuq BIF precipitated from cooling carbon-bearing fluids derived from devolatilisation reactions, which liberated CO_2 and CH_4 from pre-existing organic matter (now graphite) and precipitated it as PCG. A detailed comparative assessment with all known incidences of graphitic carbon with apatite in BIF (Supplementary Table 3), shows that PCG in other BIF may also represent devolatilised and remobilised organic material. The origins of this organic matter, however, need to be assessed on an individual basis.

3.5 Sources of carbon in graphite and testing the null hypothesis

Discounting younger rocks rich in organic matter by their absence from the Nuvvuagittuq area, the source of carbon in carbon-bearing fluids in the BIF has three possible origins: 1) mantle or sub-lithospheric CO_2 and CH_4, 2) decarbonation of carbonates and 3) devolatilisation of syngenetic organic matter (Luque et al., 2014). The graphitic carbon in the greenschist facies Brockman, Temagami, Sandur and Wutai BIF have $\delta^{13}C_{gra}$ values of -25.2‰, -27.8‰, -28.5‰, and -22.5‰ respectively. While in the amphibolite facies Pääkkö, Nuvvuagittuq and Anshan BIF, $\delta^{13}C_{gra}$ values are -19.6‰, -28.1‰ to -26.4‰, and -26.7 to -22.0‰ respectively. In the hornfels-pyroxene facies Biwabik and granulite facies Akilia BIF, the bulk rock $\delta^{13}C_{gra}$ values are, -28.1‰ and -17.5‰, respectively (Table 2). All these values fall within the average composition of sedimentary organic matter over the last 3,500 Myr (Schidlowski, 2001), except the Akilia bulk $\delta^{13}C_{gra}$ values, yet *in-situ* analyses on individual graphite coatings on apatite grains have a very large range between -4 and -49 ‰ (McKeegan et al., 2007; Mojzsis et al., 1996; Papineau et al., 2010b), which is consistent with a protracted metamorphic history. Decarbonation reactions can be ruled out, as the $\delta^{13}C_{carb}$ values for all the BIF are significantly heavier (-4.4 and -9.1‰) than $\delta^{13}C_{gra}$ values (Table 2) (Papineau et al., 2011). Additionally, Rayleigh distillation effects would only shift C isotopes toward heavier compositions (Luque et al., 2012) during precipitation of C from C-O-H fluids. Conversely, during retrograde reactions fluid compositions with CO_2 > CH_4, may shift C isotopes of precipitated graphite to lighter values (Farquhar et al., 1999). However, under typical crustal conditions, fluids are reducing and CH_4 dominates (Eiler et al., 1997). This may be especially true of BIF, which typically contain reduced mineral assemblages such as magnetite, so that, CO_2 concentrations are unlikely to have been greater than CH_4, ruling out a retrograde reaction as the origin of light C isotope compositions. Fluid-deposited graphite derived from C-O-H fluids of mantle origin are typically much heavier than -14‰ (Luque et al., 1998; Pearson et al., 1994). Moreover, we argue that meteoritic organic matter can be ruled out due to the absence of detrital or meteorite components in the BIF sediments, expected to be deposited along with meteoritic organic matter.

The production of abiotic organic matter in hydrothermal vents is known to produce isotopically light hydrocarbons, typically with less than four carbon atoms (Charlou et al., 2010; McCollom, 2013; McCollom and Seewald, 2007). The isotopic signature of these hydrocarbons are characteristically not lighter than -15 to -19‰ in natural vent sites (McDermott et al., 2015; Proskurowski et al., 2008). Yet, experimental reduction of inorganic carbon compounds such as CO, CO_2 and HCO_3^- has yielded CH_4 with isotopic compositions reaching as low as -50‰ (Horita and Berndt, 1999; McCollom and Seewald, 2007). If during metamorphism isotopically light CH_4 was produced by reduction of CO_2 in the Nuvvuagittuq or other BIF, CO_2 would also react with the CH_4 produced in order to precipitate graphite (Equ. 1). Therefore, the bulk isotopic composition of graphitic carbon in the Nuvvuagittuq BIF is equivalent to the original CO_2 reservoir of a closed system. Bulk rock powders can be used to roughly estimate the isotopic composition of crystalline graphite and PCG in the Nuvvuagittuq BIF. For example, the Nuvvuagittuq jasper-carbonate BIF samples only contain crystalline graphite (PC0822, PC0844)(Dodd et al., 2017) and have $\delta^{13}C_{org}$ values of -21.1 to -24.6‰, whereas the Nuvvuagittuq silicate BIF samples contain predominately PCG and have a similar range of $\delta^{13}C_{org}$ values of -20.6 to -26.4‰ (PC0825, Fig. 1) (Papineau et al., 2011). Further *in-situ* work is needed to precisely determine their individual carbon isotopic compositions. If these estimates for the isotopic compositions of PCG and crystalline graphite are correct, their similar isotopic composition is an expected result from liberation of CO_2 and CH_4 from a common syngenetic source of organic matter, and precipitation via equation 1 (Crespo et al., 2004). In other words, a significant amount of retrograde PCG was likely sourced from syngenetic organic matter, and this syngenetic organic matter now occurs as crystalline graphite formed during prograde metamorphism.

To further test for possible non-biological sources of organic matter (now preserved as crystalline graphite), we consider abiotic hydrocarbon synthesis in serpentinites from the Nuvvuagittuq belt. Serpentinites from the Nuvvuagittuq belt occur in ultramafic rocks, which are interpreted to be co-genetic with the Ujaraaluk amphibolite (O'Neil et al., 2011).

The composition of the Ujaraaluk amphibolite, along with the association of anthophyllite-cordierite Mg-rich rocks, is consistent with hydrothermal alteration of oceanic crust (O'Neil et al., 2011), likely responsible for the serpentinisation. Deposition of the BIF is believed to be associated with this hydrothermal activity on the seafloor. Moreover, the BIF is found between the layers of serpentinite in the belt (O'Neil et al., 2011). Pentlandite [$(Fe, Ni, Co)_9S_8$] (Supplementary Table 1) is a common mineral in these serpentinites, and believed to be an effective natural catalyst of Fischer-Tropsch reactions in natural settings (Horita and Berndt, 1999; McCollom, 2013). However, among twenty-five Raman scans over three samples, we found no organic matter associated with these minerals, nor did we find organic carbon associated with apatite and carbonate in the serpentinite (Fig. 8). To corroborate these observations, results from the analysis of bulk rock powders of the serpentinite showed no detectable organic matter (Table 2).

The serpentinites contain all the necessary ingredients for organic synthesis, including suitable catalysts (pentlandite) and a carbon source (carbonate), yet organic matter was not detected. While the analyses of three serpentinite samples is not exhaustive, as it currently stands these new observations suggest that abiotic hydrocarbon production during serpentinisation in seafloor systems was unlikely to be significant during deposition of the Nuvvuagittuq BIF. Alternatively, abiotic organic matter may not be retained in serpentinites. The restricted range of C isotopic compositions of graphitic carbon in BIF throughout the Precambrian suggests a similar C-isotope fractionation process, which is likely a biological one. We acknowledge that while modern hydrothermal vents produce abiotic organics with $\delta^{13}C$ signatures higher than that of the reported graphitic carbons, Archean hydrothermal systems may have synthesised organics with lower $\delta^{13}C$ signatures, as inferred by experiments (Horita and Berndt, 1999). Finally, the possibility of some ^{13}C-

depleted CO_2 or CH_4 infiltration into the rock during metamorphism cannot be fully excluded, but coatings of PCG on crystalline graphite, as well as similar isotopic compositions between BIF samples (Papineau et al., 2011), point to an *in-situ*, syngenetic, and sedimentary source of carbon.

4.0 Implications and conclusions

The occurrence of ^{13}C-depleted graphite associations with apatite in one of Earth's oldest BIF, and its use as a biosignature, has been a subject of controversy (Lepland et al., 2005; McKeegan et al., 2007; Mojzsis et al., 1996; Nutman and Friend, 2006). Several studies failed to find apatite + graphite mineral assemblages in the Akilia BIF, or presumed such associations to be rare (Lepland et al., 2005; Nutman and Friend, 2006). Subsequently it was found that about 25% of apatite grains were associated with graphite (Papineau et al., 2010a). The documentation of 10 different BIF, from the Eoarchaean to the Palaeoproterozoic, show the mineral association of apatite + graphite to be commonplace in BIF across various metamorphic grades. However, we did not find evidence for graphite inclusions in apatite, as previous studies have claimed (McKeegan et al., 2007; Mojzsis et al., 1996), with graphite frequently coating apatite. Graphite particles which occur in the centre of apatite grains (Fig. 3d) may be coatings in the line of sight (Papineau et al., 2010a). Yet large apatite bands in the Dales gorge BIF appear to have inclusions of kerogen (Fig. 7b), so graphite inclusions in apatite remain possible.

Apatite and graphite mineral assemblages in BIF are viewed here as having two possible origins. In greenschist facies BIF, graphitic carbon is found in sedimentary bands of carbonate and apatite. These likely represent the mineralised products of decayed biological organic matter (Li et al., 2011), as observed in the Brockman, Temagami and Sandur BIF.

These mineral associations persist into the amphibolite facies, where graphite is associated with apatite, in the Pääkkö, Anshan, and Saglek BIF (Fig. 3j-l; 6d, j). Furthermore, the occurrence of apatite and graphite from the 3,780 to 3,920 Myr Saglek BIF could provide support for previous interpretations that graphite with ^{13}C-depleted isotopic compositions from the Saglek belt represents microbial remains (Tashiro et al., 2017).

In highly metamorphosed BIF, higher temperatures may lead to cracking of kerogen, which produces significant quantities of CH_4. The association of PCG with retrograde minerals points to the fluid-deposition of apatite and PCG during retrograde metamorphism, a process that can proceed at the upper greenschist to amphibolite facies, for instance in the Anshan, Biwabik, Akilia and Nuvvuagittuq BIF (Supplementary Table 3). The fluid deposition of apatite during metamorphism may be supported by other studies which found the rare-earth element patterns of apatite from the Akilia and other Eoarchaean BIF to be consistent with a metamorphic origin (Lepland et al., 2002; Nutman and Friend, 2006). While graphitic carbon associated with apatite is commonplace in Eoarchaean to Palaeoproterozoic BIF, the possibility of their co-precipitation during metamorphism means that the null hypothesis for a biological source of carbon in graphite cannot be fully rejected. This is based on experiments that show that non-biological C-isotope fractionation overlaps the biological range, and that carbon in C-O-H fluids may include several different sources. From the detailed study of variably aged and metamorphosed BIFs, uniformitarianism suggests apatite + graphite biosignatures in Earth's oldest rocks are ambiguous indicators of life, unless they can be proven to be syngenetic and shown to be associated with other possible biosignatures, such as in the case of the Nuvvuagittuq jasper-carbonate BIF (Dodd et al., 2017). In this instance the crystalline structure of the graphite is consistent with a syngenetic origin, unlike PCG (Fig. 4; Supplementary Figure 1), and the apatite in which it sometimes occurs forms large euhedral laths, consistent with prograde apatite (Nutman, 2007). Therefore, in this case the apatite+graphite+carbonate association fits best with an origin from biomass remineralisation, as can be inferred for the Dales gorge BIF and those younger.

The new results presented here show fluid-deposited graphite is commonly associated with apatite in Earth's oldest sedimentary rocks, and therefore evidence for life's emergence on Earth rests in part on the identification of fluid-deposited and syngenetic graphite. The work here suggests that fluid-deposited carbon is partly sourced from syngenetic organic matter, the origin of which could either be pre-biotic or the remains of Earth's first lifeforms.

Acknowledgments

M.S.D. and D.P. acknowledge support from UCL and the LCN, and a DTG from EPSRC, UK. D.P. also thanks the NASA Astrobiology Institute (Grant No. NNA04CC09A), the Carnegie Institution of Washington and Carnegie of Canada for funding field work, and the Geological Survey of Western Australia, of Michigan and of Finland for access and support in the core libraries. We warmly thank B. French and A. Nutman for generously providing samples of BIF from the Biwabik and Akilia, respectively, and for insightful discussions that benefited this manuscript. We are grateful to the municipality of Inukjuak, Québec, and the Pituvik Landholding Corporation for permission to work on their territory, and to M. Carroll for logistical support. Z.S. acknowledge financial support from the National Natural Science Foundation of China (grant # 41272038) for field work in the Wutai Group of China. We also thank G. Hao and J. Xue for assistance with field trip in Wutai, J. Davy for assistance with sample preparation and SEM analyses, and Derek Vance for helping refine the letter. CM is grateful to Director, NGRI for permitting to publish this work and acknowledge MoES /P.O.(Geosciences)/08/2013 for providing the project funds.

References

Arita, Y., and Wada, H., 1990, Stable isotopic evidence for migration of metamorphic fluids along grain boundaries of marbles Geochemical Journal, v. 24, no. 3, p. 173-186.

Beyssac, O., Goffe, B., Chopin, C., and Rouzaud, J. N., 2002, Raman spectra of carbonaceous material in metasediments: a new geothermometer: Journal of metamorphic geology, v. 20, p. 859–871.

Beyssac, O., Goffé, B., Petitet, J.-P., Froigneux, E., Moreau, M., and Rouzaud, J.-N., 2003, On the characterization of disordered and heterogeneous carbonaceous materials by Raman spectroscopy: Spectrochimica Acta Part A: Molecular and Biomolecular Spectroscopy, v. 59, no. 10, p. 2267-2276.

Charlou, J. L., Donval, J. P., Konn, C., Ondréas, H., and Fouquet, Y., 2010, High production and fluxes of H2 and CH4 and evidence of abiotic hydrocarbon synthesis by serpentinization in ultramafic-hosted hydrothermal systems on the Mid-Atlantic Ridge, *in* Peter A. Rona, C. W. D., Jérôme Dyment, Bramley J. Murton, ed., Diversity of Hydrothermal Systems on Slow Spreading Ocean Ridges: Washington D.C, American Geophysical Union, p. 265-296.

Crespo, E., Luque, F. J., Barrenechea, J. F., and Rodas, M., 2005, Mechanical graphite transport in fault zones and the formation of graphite veins: Mineralogical magazine, v. 69, no. 4, p. 463-470.

Crespo, E., Luque, J., FernÁNdez-RodrÍGuez, C., Rodas, M., DÍAz-Azpiroz, M., FernÁNdez-Caliani, J. C., and Barrenechea, J. F., 2004, Significance of graphite occurrences in the Aracena Metamorphic Belt, Iberian Massif: Geological Magazine, v. 141, no. 6, p. 687-697.

Dodd, M. S., Papineau, D., Grenne, T., Slack, J. F., Rittner, M., Pirajno, F., O'Neil, J., and Little, C. T. S., 2017, Evidence for early life in Earth's oldest hydrothermal vent precipitates: Nature, v. 543, no. 7643, p. 60-64.

Dodd, M. S., Papineau, D., She, Z., Fogel, M. L., Nederbragt, S., and Pirajno, F., 2018, Organic remains in late Palaeoproterozoic granular iron formations and implications for the origin of granules: Precambrian Research, v. 310, p. 133-152.

Eiler, J. M., Mojzsis, S. J., and Arrhenius, G., 1997, Carbon isotope evidence for early life: Nature, v. 386, p. 665.

Farquhar, J., Hauri, E., and Wang, J., 1999, New insights into carbon fluid chemistry and graphite precipitation: SIMS analysis of granulite facies graphite from Ponmudi, South India: Earth and Planetary Science Letters, v. 171, no. 4, p. 607-621.

French, B. M., 1966, Some geological implications of equilibrium between graphite and a C‐H‐O gas phase at high temperatures and pressures: Reviews of Geophysics, v. 4, no. 2, p. 223-253.

Gaillard, N., Williams-Jones, A. E., Clark, J. R., Lypaczewski, P., Salvi, S., Perrouty, S., Piette-Lauzière, N., Guilmette, C., and Linnen, R. L., 2018, Mica composition as a vector to gold mineralization: Deciphering hydrothermal and metamorphic effects in the Malartic district, Quebec: Ore Geology Reviews, v. 95, p. 789-820.

Horita, J., and Berndt, M. E., 1999, Abiogenic methane formation and isotopic fractionation under hydrothermal conditions: Science, v. 285, p. 1055-1057.

Klein, C., 2005, Some Precambrian banded iron-formations (BIFs) from around the world: Their age, geologic setting, mineralogy, metamorphism, geochemistry, and origins: American Mineralogist, v. 90, no. 10, p. 1473-1499.

Kribek, B., Sykorova, I., Machovic, V., and Laufek, F., 2008, Graphitization of organic matter and fluid-deposited graphite in Palaeoproterozoic (Birimian) black shales of the Kaya-Goren greenstone belt (Burkina Faso, West Africa): Journal of Metamorphic Geology, v. 26, no. 9, p. 937-958.

Large, D. J., Christy, A. G., and Fallick, A. E., 1994, Poorly crystalline carbonaceous matter in high grade metasediments: implications for graphitisation and metamorphic fluid compositions: Contributions to Mineralogy and Petrology, v. 116, p. 108-116.

Lepland, A., Arrhenius, G., and Cornell, D., 2002, Apatite in early Archean Isua supracrustal rocks, southern West Greenland: its origin, association with graphite and potential as a biomarker: Precambrian Research, v. 118, p. 221-241.

Lepland, A., van Zuilen, M. A., Arrhenius, G., Whitehouse, M. J., and Fedo, C. M., 2005, Questioning the evidence for Earth's earliest life—Akilia revisited: Geology, v. 33, no. 1, p. 77.

Lepland, A., van Zuilen, M. A., and Philippot, P., 2011, Fluid-deposited graphite and its geobiological implications in early Archean gneiss from Akilia, Greenland: Geobiology, v. 9, no. 1, p. 2-9.

Li, Y. L., Konhauser, K. O., Cole, D. R., and Phelps, T. J., 2011, Mineral ecophysiological data provide growing evidence for microbial activity in banded-iron formations: Geology, v. 39, no. 8, p. 707-710.

Li, Y. L., Sun, S., and Chan, L. S., 2012, Phosphogenesis in the 2460 and 2728 million-year-old banded iron formations as evidence for biological cycling of phosphate in the early biosphere: Ecol Evol, v. 3, no. 1, p. 115-125.

Luque, F. J., Crespo-Feo, E., Barrenechea, J. F., and Ortega, L., 2012, Carbon isotopes of graphite: Implications on fluid history: Geoscience Frontiers, v. 3, no. 2, p. 197-207.

Luque, F. J., Huizenga, J. M., Crespo-Feo, E., Wada, H., Ortega, L., and Barrenechea, J. F., 2014, Vein graphite deposits: geological settings, origin, and economic significance: Mineralium Deposita, v. 49, no. 2, p. 261-277.

Luque, F. J., Pasteris, J. D., Wopenka, B., Rodas, M., and Barrenechea, J. F., 1998, Natural fluid-deposited graphite: mineralogcial characteristics and mechanisms of formation: American Journal of Science, v. 298, p. 471-498.

Luque, F. J., and Rodas, M., 1999, Constraints on graphite crystallinity in some Spanish fuid-deposited occurrences from different geologic settings: Mineralium Deposita, v. 34, p. 215-219.

Marshall, A. O., Emry, J. R., and Marshall, C. P., 2012, Multiple generations of carbon in the apex chert and implications for preservation of microfossils: Astrobiology, v. 12, no. 2, p. 160-166.

McCollom, T. M., 2013, Laboratory Simulations of Abiotic Hydrocarbon Formation in Earth's Deep Subsurface, *in* Hazen, R. M., Jones, A. P., and Baross, J. A., eds., Carbon in Earth, Volume 75: Virginia Mineralogical Society of America p. 467-490.

McCollom, T. M., and Seewald, J. S., 2007, Abiotic Synthesis of Organic Compounds in Deep-Sea Hydrothermal Environments: Chemical reviews, v. 107, no. 2, p. 382-401.

McDermott, J. M., Seewald, J. S., German, C. R., and Sylva, S. P., 2015, Pathways for abiotic organic synthesis at submarine hydrothermal fields: Proceedings of the national academy of science, v. 112, no. 25, p. 7668–7672.

McKeegan, K. D., Kudryavtsev, A. B., and Schopf, J. W., 2007, Raman and ion microscopic imagery of graphitic inclusions in apatite from older than 3830 Ma Akilia supracrustal rocks, west Greenland: Geology, v. 35, no. 7, p. 591.

Mojzsis, S. J., Arrhenius, G., McKeegan, K. D., Harrison, T. M., Nutman, A. P., and Friend, C. R. L., 1996, Evidence for life on Earth before 3,800 million years ago: Nature, v. 384, p. 55-59.

Nutman, A. P., 2007, Apatite recrystallisation during prograde metamorphism, Cooma, southeast Australia: implications for using an apatite – graphite association as a biotracer in ancient metasedimentary rocks: Australian Journal of Earth Sciences, v. 54, no. 8, p. 1023-1032.

Nutman, A. P., and Friend, C. R. L., 2006, Petrography and geochemistry of apatites in banded iron formation, Akilia, W. Greenland: Consequences for oldest life evidence: Precambrian Research, v. 147, no. 1-2, p. 100-106.

O'Neil, J., Francis, D., and Carlson, R. W., 2011, Implications of the Nuvvuagittuq Greenstone Belt for the Formation of Earth's Early Crust: Journal of Petrology, v. 52, no. 5, p. 985-1009.

Papineau, D., De Gregorio, B., Fearn, S., Kilcoyne, D., McMahon, G., Purohit, R., and Fogel, M., 2016, Nanoscale petrographic and geochemical insights on the origin of the Palaeoproterozoic stromatolitic phosphorites from Aravalli Supergroup, India: Geobiology, v. 14, no. 1, p. 3-32.

Papineau, D., De Gregorio, B. T., Cody, G. D., Fries, M. D., Mojzsis, S. J., Steele, A., Stroud, R. M., and Fogel, M. L., 2010a, Ancient graphite in the Eoarchean quartz–pyroxene rocks from Akilia in southern West Greenland I: Petrographic and spectroscopic characterization: Geochimica et Cosmochimica Acta, v. 74, no. 20, p. 5862-5883.

Papineau, D., De Gregorio, B. T., Cody, G. D., O'Neil, J., Steele, A., Stroud, R. M., and Fogel, M. L., 2011, Young poorly crystalline graphite in the >3.8-Gyr-old Nuvvuagittuq banded iron formation: Nature Geoscience, v. 4, no. 6, p. 376-379.

Papineau, D., De Gregorio, B. T., Stroud, R. M., Steele, A., Pecoits, E., Konhauser, K., Wang, J., and Fogel, M. L., 2010b, Ancient graphite in the Eoarchean quartz-pyroxene rocks from Akilia in southern West Greenland II: Isotopic and chemical compositions and comparison with

Paleoproterozoic banded iron formations: Geochimica et Cosmochimica Acta, v. 74, no. 20, p. 5884-5905.

Pasteris, J. D., 1999, Causes of the uniformly high crystallinity of graphite in large epigenetic deposits: Journal of metamorphic geology, v. 17, p. 779-787.

Pasteris, J. D., and Chou, I.-M., 1998, Fluid-deposited graphitic inclusions in quartz: Comparison between KTB (German Continental Deep-Drilling) core samples and artificially reequilibrated natural inclusions: Geochimica Et Cosmochimica Acta, v. 62, no. 1, p. 109-122.

Pearson, D. G., Boyd, F. R., Haggerty, S. E., Pasteris, J. D., Field, S. W., Nixon, P. H., and Pokhilenko, N. P., 1994, The characterisation and origin of graphite in cratonic lithospheric mantle: a petrological carbon isotope and Raman spectroscopic study: Contributions to Mineralogy and Petrology, v. 115, p. 449-466.

Proskurowski, G., Lilley, M. D., Seewald, J. S., Früh-Green, G. L., Olson, E. J., Lupton, J. E., Sylva, S. P., and Kelley, D. S., 2008, Abiogenic hydrocarbon production at Lost City hydrothermal field: Science, v. 319, p. 604-607.

Satish-Kumar, M., Jaszczak John, A., Hamamatsu, T., and Wada, H., 2011, Relationship between structure, morphology, and carbon isotopic composition of graphite in marbles: Implications for calcite-graphite carbon isotope thermometry, American Mineralogist, Volume 96, p. 470.

Schidlowski, M., 2001, Carbon isotopes as biogeochemical recorders of life over 3.8 Ga of Earth history: evolution of a concept: Geochimica Et Cosmochimica Acta, v. 106, p. 117-134.

She, Z.-B., Strother, P., and Papineau, D., 2014, Terminal Proterozoic cyanobacterial blooms and phosphogenesis documented by the Doushantuo granular phosphorites II: Microbial diversity and C isotopes: Precambrian Research, v. 251, p. 62-79.

Tashiro, T., Ishida, A., Hori, M., Igisu, M., Koike, M., Mejean, P., Takahata, N., Sano, Y., and Komiya, T., 2017, Early trace of life from 3.95 Ga sedimentary rocks in Labrador, Canada: Nature, v. 549, no. 7673, p. 516-518.

Valley, J. W., and O'Neil, J. R., 1981, 13C12C exchange between calcite and graphite: A possible thermometer in Grenville marbles: Geochimica et Cosmochimica Acta, v. 45, no. 3, p. 411-419.

van Zuilen, M. A., Fliegel, D., Wirth, R., Lepland, A., Qu, Y., Schreiber, A., Romashkin, A. E., and Philippot, P., 2012, Mineral-templated growth of natural graphite films: Geochimica et Cosmochimica Acta, v. 83, p. 252-262.

Wang, A., Dhamenincourt, P., Dubessy, J., Guerard, D., Landais, P., and Lelaurain, M., 1989, Characterization of graphite alteration in an uranium deposit by micro-Raman spectroscopy, X-ray diffraction, transmission electron microscopy and scanning electron microscopy: Carbon, v. 27, no. 2, p. 209-218.

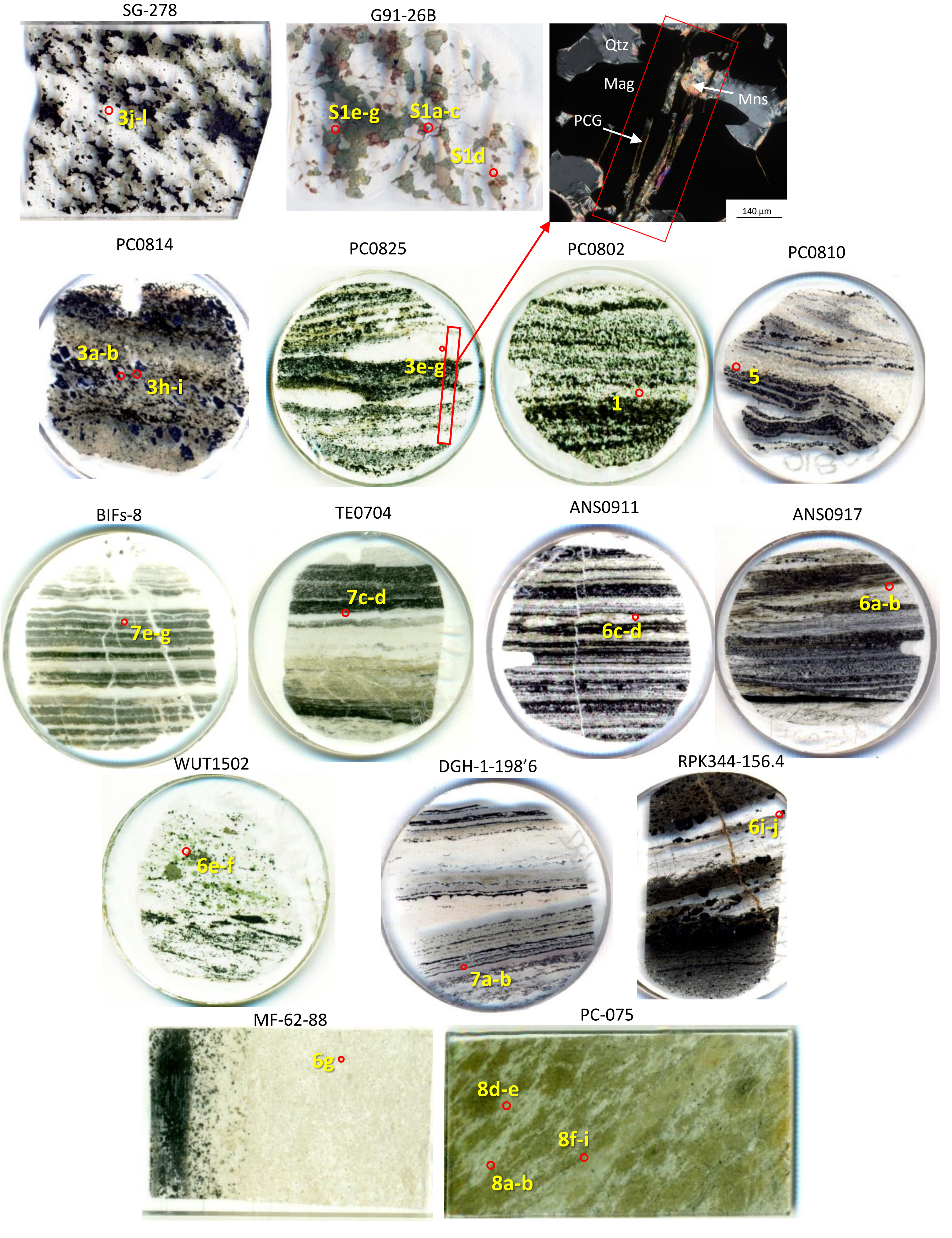

Figure 1. Thin section scans of samples in this study. SG-278 – Saglek BIF. G91-26B – Akilia quartz-pyroxene rock. PC0814, PC0825 (red box = graphite vein), CP image of poorly crystalline graphite and minnesotaite vein cutting magnetite bands. PC0802, PC0810 – Nuvvuagittuq BIF. ANS0911, ANS0917 – Anshan BIF. WUT1502 – Wutai BIF. BIFs-8 – Sandur BIF. DGM-1-198’6 – Brockman, Dales Gorge BIF. TE0704 – Temagami. RPK344-156.4 – Pääkkö. MF-62-88 – Mesabi BIF. PC-075 – Nuvvuagittuq serpentinite. All round sections are 2.5cm in diameter. Rectangle section are 2.5cm wide.

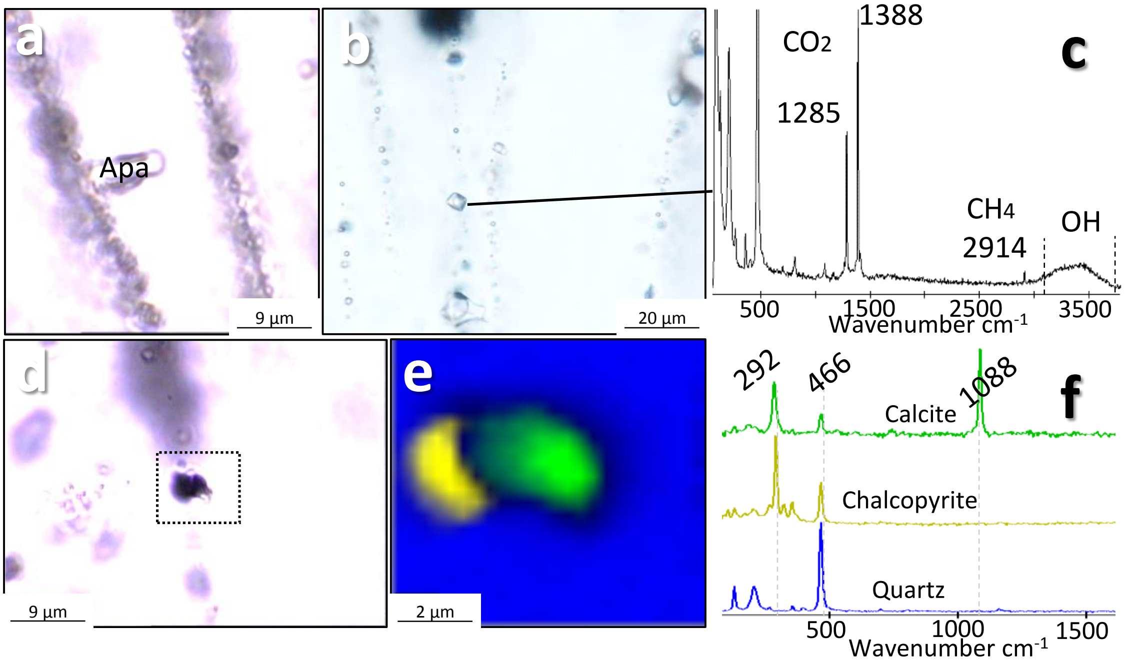

Figure 2. Fluid inclusions in the Nuvvuagittuq BIF, PC0802. a) Transmitted light image of apatite with fluid inclusion trails. b) CO_2-CH_4-H_2O bearing fluid inclusions. c) Raman spectrum of fluid inclusion in b. d) Transmitted light image of calcite and chalcopyrite with fluid inclusion trail. e) Raman map showing calcite with chalcopyrite in fluid inclusion trail. f) Raman spectra for Raman map in e. Apa – apatite. Raman map colours: green – calcite, yellow – chalcopyrite, blue – quartz.

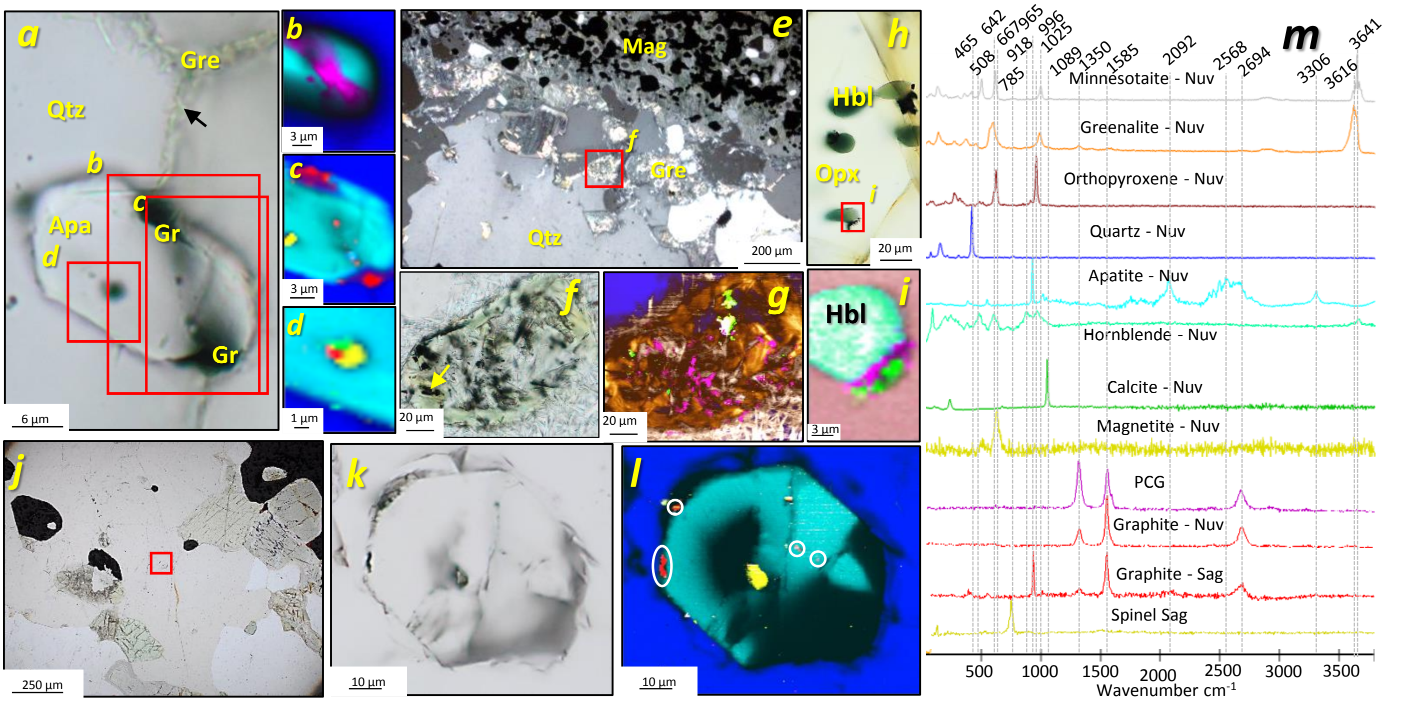

Figure 3. Graphitic carbon associations in the Eoarchean-Hadean Nuvvuagittuq and Saglek BIF. a) Plane Polarised Light (PPL) image of apatite associated with multiple crystallinities of graphitic carbon, arrow points to greenalite filling cracks. b) Raman map of boxed area in panel b taken at a confocal depth of 5 µm. c-d) Raman maps of boxed areas in *a* at surface of thin section. e) Cross Polars (CP) image of greenalite between quartz grains. f) PPL image of greenalite cluster surrounded by minnesotaite (arrow points to sulphide grain). g) Raman map showing PCG associated with calcite inside the greenalite cluster. h) PPL image of orthopyroxene with inclusions of ferro-hornblende i) Raman map of PCG and calcite coating hornblende. j) PPL image of apatite location in the Saglek BIF, red box corresponds to panel k. k) PPL image of apatite with opaque inclusions and coatings. l) Raman image of panel k, showing graphite within and on the edges of the apatite grain (white circles), including an inclusion of spinel. m) Raman spectra for this figure. Mineral abbreviations: Apa – apatite, Gr – graphite, Gre – greenalite, Qtz – quartz, Mag – magnetite, Hbl – hornblende, Opx - orthopyroxene. Raman map colours: grey – minnesotaite, orange – greenalite, brown, orthopyroxene, blue – quartz, turquoise – apatite, light green – hornblende, green – calcite, yellow – magnetite (spinel – Saglek sample), purple – poorly crystalline graphite, red – crystalline graphite.

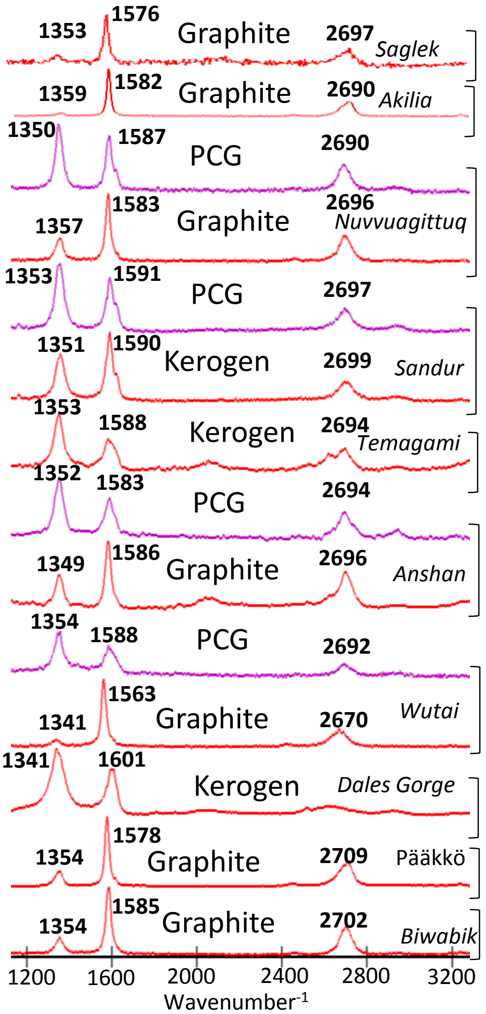

Figure 4. Crystallinities of graphitic carbon in Archean and Palaeoproterozoic BIFs in order or decreasing age. Purple colour corresponds to poorly crystalline graphite (PCG) co-occurring with graphite. PCG is defined as having an intense D-peak (~1350 cm^{-1}) relative to the G-peak (~1580 cm^{-1}) and is distinguished from kerogen by the presence of a sharp 2D peak (~2700 cm^{-1}).

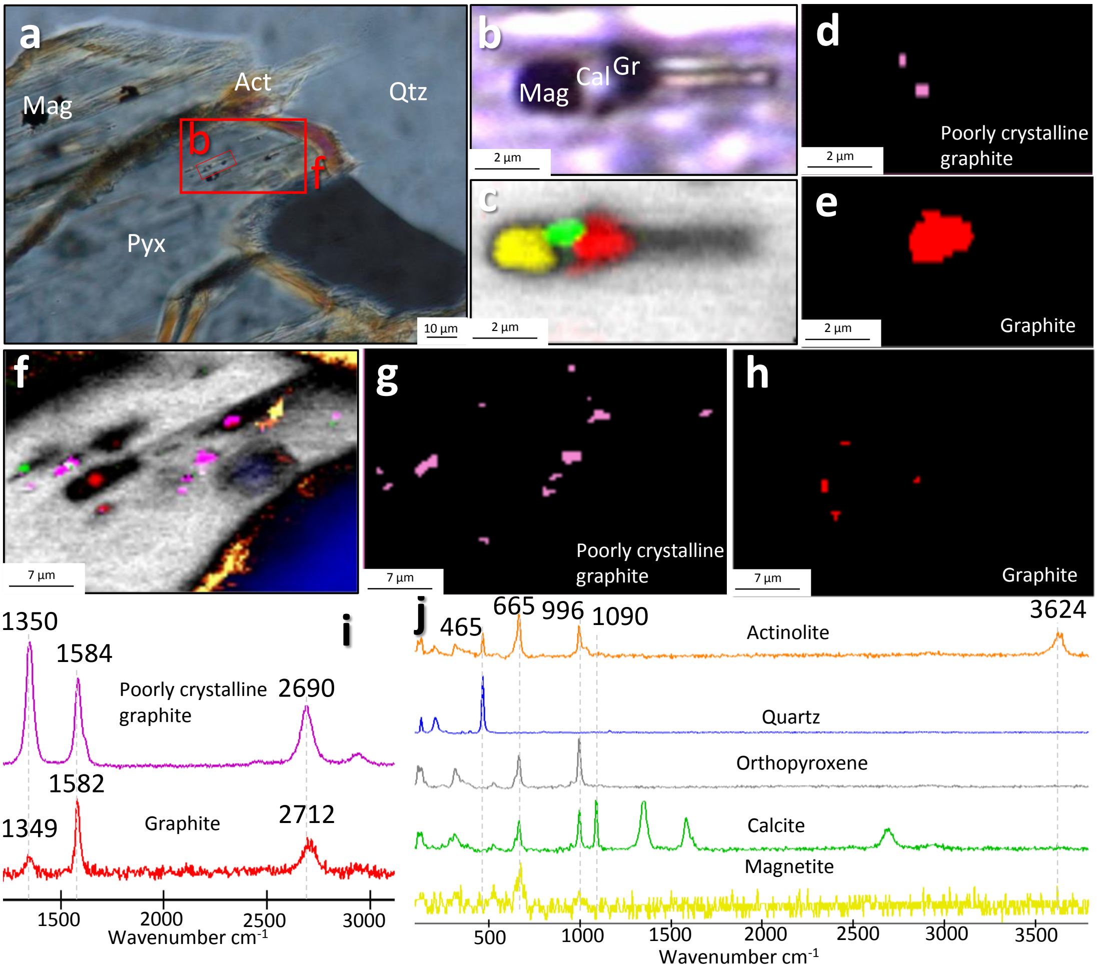

Figure 5. Crystalline and poorly crystalline graphite in the Nuvvuagittuq BIF, PC0810. a) Cross polar image of pyroxene with serpentinised edges (orange); red boxes mark Raman maps. b) Transmitted light image of magnetite, carbonate and graphitic carbon in pyroxene. c) Raman map of magnetite, calcite and graphitic carbon in orthopyroxene. d-e) Raman filter map showing the intimate association of graphite and PCG. f) Raman map showing PCG, graphite and calcite in orthopyroxene. g-h) Raman filter map showing the close spatial association of PCG and graphite in f. i) Raman spectra of graphitic carbon in pyroxene. j) Representative Raman spectra for the figure. Pyx- pyroxene, Act – actinolite, Qtz – quartz. Raman map colours: grey –orthopyroxene, orange – actinolite, blue – quartz, green – calcite, yellow – magnetite, purple – poorly crystalline graphite, red – crystalline graphite.

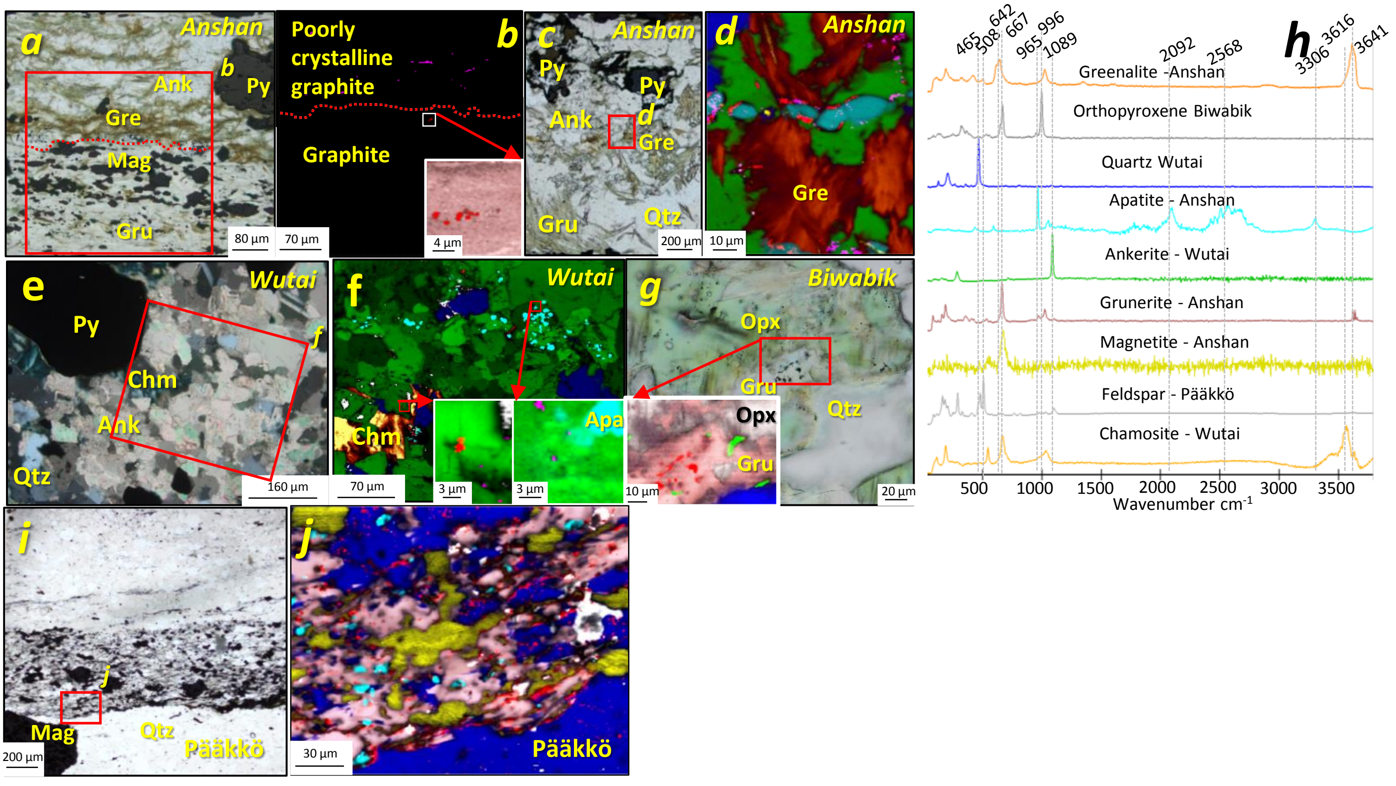

Figure 6. Graphitic carbon in strongly metamorphosed BIFs. a) PPL image of grunerite and magnetite layers in the Anshan BIF. b) Graphite filter map showing the localised occurrences of PCG and graphite. c) PPL image of grunerite and pyrite layer in the Anshan BIF. d) Raman map of apatite with coatings of graphite, along with surrounding PCG and greenalite. e) CP image of ankerite and pyrite layer in the Wutai BIF. f) Raman showing the close association of PCG and graphite and PCG with apatite. g) PPL image of clinopyroxene exhibiting grunerite rims with inclusions of graphitic carbon in the Biwabik BIF. h) Raman spectra for this figure. i) PPL image of grunerite-magnetite layer in the Pääkkö BIF. j) Raman map showing the association of graphite with apatite and grunerite. Mineral abbreviations: Ank – ankerite, Gru – grunerite, Py – pyrite, Chm – chamosite. Raman map colours: grey – orthopyroxene (Biwabik)/ feldspar (Pääkkö) , orange – greenalite (Anshan)/ chamosite (Wutai), brown - grunerite, blue – quartz, turquoise – apatite, green – ankerite, yellow – magnetite, purple – poorly crystalline graphite, red – crystalline graphite. See Fig. 3 for graphite spectra.

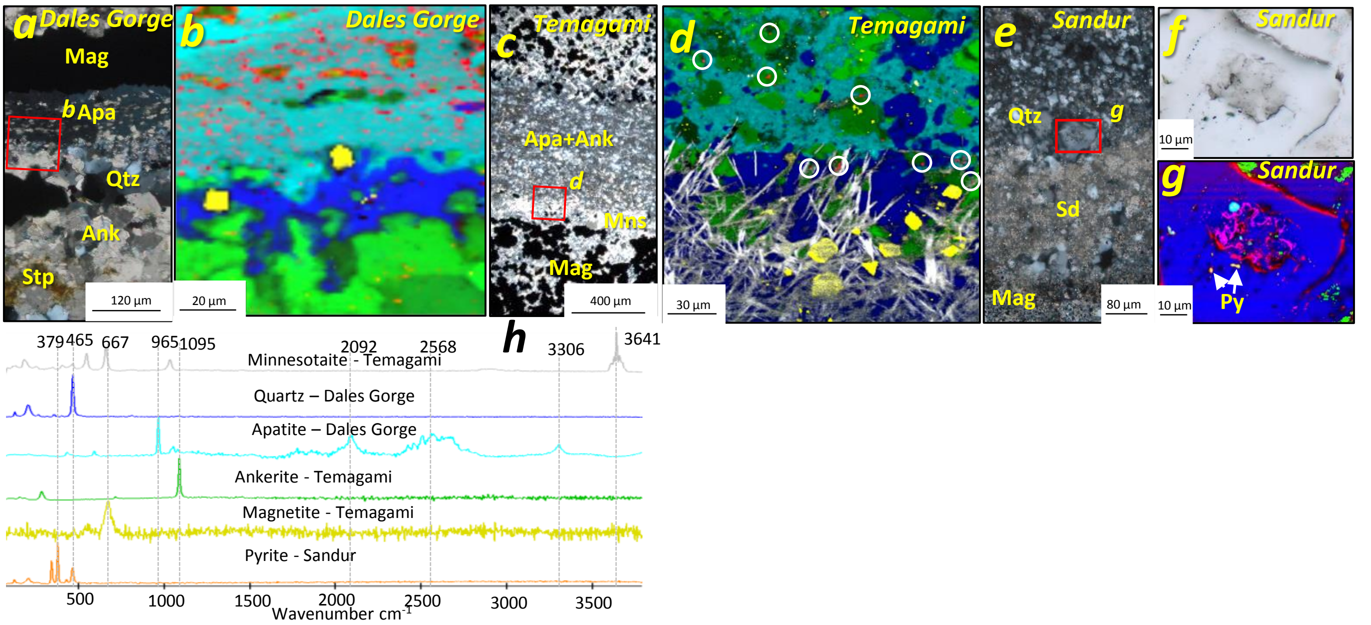

Figure 7. Graphitic carbon and apatite in weakly metamorphosed BIFs. a) CP image of magnetite and apatite bands in the Dales Gorge BIF, box corresponds to b. b) Raman map of graphitic carbon in apatite. c) CP image of apatite band with ankerite in the Temagami BIF, box corresponds to d. d) Raman map of apatite band with ankerite and graphitic carbon inclusions (circled). e) CP image of siderite and magnetite band in the Sandur BIF, box corresponds to f. f) PPL image of inclusions in quartz. g) Raman map of graphite and PCG associated with apatite and pyrite. h) Raman spectra for this figure. Raman map colours: grey – minnesotaite, orange – pyrite, blue – quartz, turquoise – apatite, green – ankerite, yellow – magnetite, purple – poorly crystalline graphite, red – crystalline graphite. See Fig. 3 for graphite spectra.

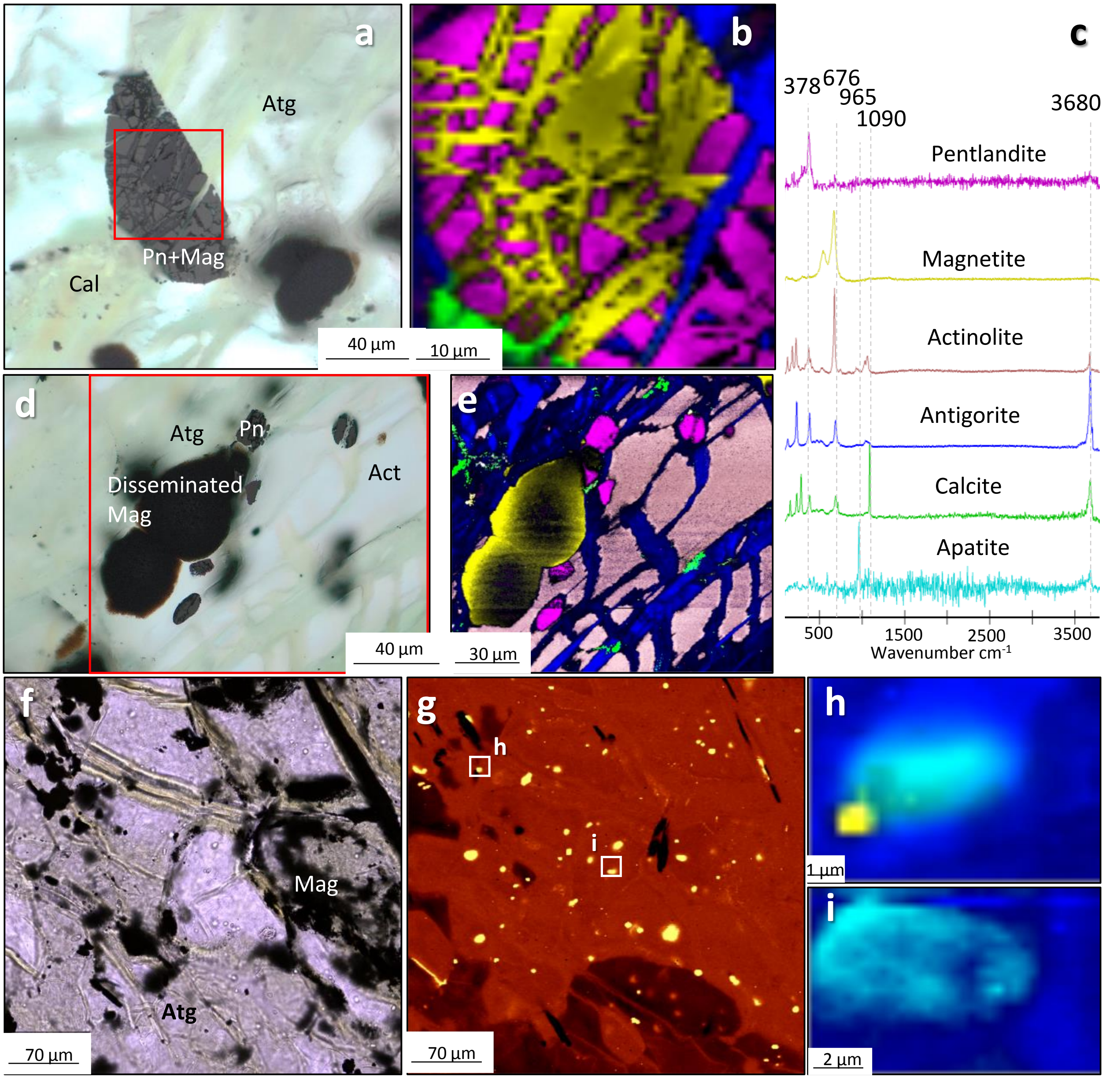

Figure 8. Selected targets from serpentinite rocks associated with the Nuvvuagittuq BIF, PC-075. a) PPL image of pentlandite-magnetite crystal in a matrix of antigorite and carbonate. b) Raman map of pentlandite and magnetite grain with calcite. c) Representative Raman spectra for this figure. d) PPL image of magnetite associated with pentlandite in serpentinite. e) Raman map pentlandite and magnetite grains show no association with reduced carbon in the presence of calcite. f) PPL image of serpentinite with magnetite and apatite crystals. g) Raman map for filter 965 cm^{-1} shows apatite distribution, boxes correspond to h-i. h-i) Raman map of apatite from panel e show no graphitic carbon associations. Pn – pentlandite, Atg – antigorite, Cal – calcite, Mag- magnetite. Raman map colours: brown - actinolite, blue – quartz, turquoise – apatite, green – calcite, yellow – magnetite, purple – pentlandite

Table 1. Summarised details of the BIF samples included in this study. See supplementary information for detailed review of the samples.

Banded iron formation	Location	Age (Myr)	Metamorphic facies	Associated lithologies	Mineralogy of iron formation
Saglek	N58 23 53.13 W63 6 41.85	3, 780-3, 920	Amphibolite	Mafic volcanics, pelitic rocks, carbonate rocks, conglomerate, chert, ultramafic rocks	Qtz-mag-pyx-apa
Akilia	N63 55 40 W51 41 30	>3,830	Granulite	Mafic amphibolite and ultramafic rocks, leucogranite, quartzofeldspathic orthogniess	Qtz-pyx-hbl-sulphides-cal-apa-gra
Nuvvuagittuq	**PC0802** - N58 16 43.5 W77 43 57.7 **PC0810-** N58 18 07.4 W77 43 51.2 **PC0814** - N58 17 12.3 W77 44 11.6 **PC0825** - N58 17 08.7 W77 44 12.2 **PC-014** - N58 17 50.22 W77 44 10.09 **PC-075** - 58 17 33.4 W77 44 2.34 **PC-091** N58 17 31.57 W77 44 6.44	4,280-3,770	Amphibolite	Amphibolite, orthogniess, chlorite meta-volcanics, serpentinite, ultra-mafics, quartz-biotite schist, fuschite silica formation, conglomerate	Qtz-mag-pyx-gru-gre-apa-gra
Sandur	N 15 06 19 W 76 34 50	Ca. 2,700	Greenschist	Conglomerate, greywacke, intermediate-acid volcanics, granite	Qtz-mag-sd-py-silicates-apa-gra
Temagami	Sherman mine, Ontario	Ca. 2,700	Greenschist	Mafic volcanics and turbidites	Qtz-mag-ank-mns-apa-gra
Anshan	Drill core taken several kilometres south east of Qidashan, Liaoning province	Ca. 2,550	Amphibolite	Metavolcanic amphibolite, fine-grained biotite gneiss, quartzite, phyllite and schists	Qtz-mag-gru-ank-gre-py-apa-gra
Wutai – Baizhiyan fm.	Puhsang mine, Shanxi province	Ca. 2,500	Greenschist	Chlorite-actinolite schist, intermediate-felsic volcanics	Qtz-mag-ank-py-chm-apa-gra
Dales Gorge	DGH-1 drill core	Ca. 2,500	Lower greenschist	Shale	Qtz-mag-sd-mns-stp-hem-apa-gra
Pääkkö	Drill core #344 - M-52/3441/73/344	1,920-2,000	Low amphibolite	Dolomites-black shale, phyllite, metadiabase, quartzite	Qtz-mag-py-gru-ab-gra
Biwabik	47.68 N 91.88 W	Ca. 1,880	Granulite	Quartzite	Qtz-pyx-mag-gru-gra

Mineral abbreviations: Qtz – quartz, mag – magnetite, py – pyrite, pyx – pyroxene, gru – grunerite, gra – graphite, apa – apatite, stp – stilpnomelane, hem – haematite, sd – siderite, mns – minnesotaite, chm – chamosite, gre – greenalite, ank – ankerite, hbl – hornblende, cal – calcite, ab - albite

Table 2. Stable isotope compositions of OM and carbonate in bulk rock powders of BIFs in this study. †Denotes data taken from Papineau et al., 2010b. bdl – below detection limit, *organic and acid insoluble mineral extract. Samples weighed between 30-60mg for organic analyses.

Sample name	**TOC %**	$\delta^{13}C_{org}$ **(VPDB) ‰**	$\delta^{13}C_{Carb}$ **(VPBD) ‰**	$\delta^{18}O_{Carb}$ **(SMOW) ‰**
G91-26C Akilia†	0.01	-17.5	-4.4	+14.0
PC0814 (NSB)	0.03	-28.1	bdl	bdl
PC0825 (NSB)	0.05	-26.4	-7.0	+18.5
PC-075 (NSB)	bdl	bdl	-4.9	+15.5
PC-014 (NSB)	bdl	bdl	bdl	bdl
PC-091 (NSB)	bdl	bdl	-4.5	+16.5
BIFs-8 (Sandur)	0.21*	-28.5	-9.5	+17.3
TE0704 (Temagami)	0.04	-27.8	-4.6	+15.7
ANS0911 (Anshan)	0.03	-22.0	-7.3	+14.5
ANS0917 (Anshan)	0.03	-26.7	-8.2	+14.5
WUT1512 (Wutai)	0.05	-22.5	-3.4	+10.5
DGM-1-198-6 (Dales Gorge)	0.03	-25.2	-10.3	+19.9
MF-62-88 (Biwabik)	0.03	-28.4	bdl	bdl
PK344-156.4 (Pääkkö)	0.45	-19.6	-3.7	+21.0

Sample descriptions

Saglek block

The Saglek-Hebron gneiss complex, located in Northern Labrador (Canada), contains supracrustal rocks comprising metasedimentary rocks including pelitic, carbonate, conglomerate and BIF lithologies, along with various mafic volcanic rocks and ultramafic lithologies. The structural setting and stratigraphic successions of the Saglek complex have been taken to suggest it represents an accretionary complex (Komiya et al., 2015). Uranium-Pb ages on zircons from gneisses have yielded up to 3920 ± 49 Myr, the oldest age currently found in the complex (Shimojo et al., 2016). These gneisses have been interpreted to intrude the supracrustal rocks and therefore would represent a minimum age for the supracrustal rocks. Younger ages for these rocks have however also been proposed, ranging between 3612 ± 130 Myr (Re-Os, Ishikawa et al., 2017) and 3782 ± 93 Myr (Sm-Nd, Morino et al., 2017). The complex has undergone a complicated protracted thermal history with several magmatic and metamorphic episodes (Komiya et al. 2017; Kusiak et al. 2017). The peak of metamorphism reached upper amphibolite to granulite facies occurred around 2600 to 2700 Myr (Schiøtte et al., 1989; Wendt and Collerson, 1999).

Akilia Quartz-pyroxene rock association

The protolith of the Akilia Quartz-pyroxene (Qp) rock was originally interpreted to be silicate iron formation (Manning et al., 2006; Nutman et al., 1997) however some view the rock as having formed as a result of metasomatic alteration of an ultramafic protolith (André et al., 2006; Fedo and Whitehouse, 2002). A detailed analysis of the evidence for a chemical sedimentary origin of the Akilia Qp rocks was previously presented (Manning et al., 2006). Age constraints of the Qp rock were initially determined to be >3850 Myr based on U–Pb zircon geochronology on neighbouring orthogneisses to the enclave (Nutman et al., 1997), but this also has been the subject of debate (Whitehouse and Kamber, 2005). Ages for the zircons summarized in (Manning et al., 2006) are consistent with the metamorphic history of other rocks in the vicinity of Akilia (Nutman et al., 2002). The complex was metamorphosed to the upper amphibolite-granulite facies between 3660-3650 Myr, with a stronger amphibolite-granulite metamorphic event at 3590-3550 Myr followed by ductile deformation and upper amphibolite metamorphic events from 2730-2550 Myr (Nutman et al., 2002).

Nuvvuagittuq supracrustal belt

The Nuvvuagittuq Supracrustal Belt (NSB) was mostly metamorphosed to upper amphibolite facies with temperatures reaching 650°C and 4-5 Kbars (Cates and Mojzsis, 2009; O'Neil et al., 2007). Sm-Nd isotopic compositions of garnets and U-Pb data in metamorphic zircons in the NSB amphibolites suggests that the peak metamorphic event occurred in the Neoarchean (Darling et al., 2013; O’Neil et al., 2012) contemporaneous with the intrusion of pegmatites dated at 2688 ± 2 Myr (David et al., 2009). This is also consistent with the regional metamorphism occurring at 2705 – 2680 Myr (Boily et al., 2009). The amphibolites to the southwest and southeast corners of the NSB are characterized by lower metamorphic grade assemblages of chlorite-epidote-actinolite. To the southeast, chlorite preserves the shape of what appears to have been garnet crystals, suggesting that the lower greenschist assemblage is retrograde (O'Neil et al., 2007). No evidence of retrogressed garnet are observed in the lower grade facies to the SW which may never have reached the upper amphibolite facies. The geochronology of the NSB is highly debated and two ages have been proposed for the NSB metavolcanic rocks: an Eoarchean age of ~3800 Myr (Cates et al., 2013; Guitreau et al. 2013; Roth et al. 2013) and a Hadean age of ~4300 Myr (O’Neil et al., 2008; O’Neil et al., 2012). Details about the age debate of the NSB metavolcanic rocks are reviewed in O’Neil et al. (2019).

Sandur superterrane

The Sandur Superterrane underwent three phases of deformation (Mukhopadhyay and Matin, 1993) and the metamorphic grade varies from greenschist to upper amphibolite facies, depending on the terrane. U-Pb age of zircons from the Eastern Felsic Volcanic Terrane (EFVT) give an age of 2700 Myr (Nutman et al., 1996), additionally a Sm-Nd date for the Sultanpura Volcanic Terrane komatiites gives 2700 Myr (Naqvi et al., 2002). The supracrustal terranes have been intruded by a series of granitoids after their accretion, of which one granitoid from the EFVT has been dated at 2719±40Myr (Nutman et al., 1996). Studies suggested the belt has undergone 7-8 times crustal shortening due to horizontal compression as a consequence of convergent margin tectonism (Manikyamba and Naqvi, 1996).

Temagami greenstone belt

Temargami BIF was collected from tailings inside the Sherman mine Ontario. The BIF is associated with basalt and turbidites. The regional metamorphic grade is greenschist. The Iceland Lake pluton and a nearby rhyolite flow stratigraphically below the BIF are contemporaneous and yield ages of 2736±2Myr and 2736±3Myr respectively; the youngest plutonic activity is the emplacement of a late rhyolite porphyry dike at 2687±2Myr (Bowins and Heaman, 1991).

Anshan supracrustal group

Anshan is located in the Anshan-Benxi area with the largest BIF iron resource in the North China Craton (Wan et al., 2016). Zircon U-Pb dating shows that magmatic zircons from metavolcanic rocks in the Anshan area, were recrystallized at 2551±10 Myr, representing the formation age of the Anshan BIF, while the metamorphic zircons were formed at 2469±23 Myr, reflecting the age of the later metamorphic event (Dai et al., 2013). U-Pb zircon dating on 12 supracrustal samples of the Anshan Group from the Anshan-Benxi area, gives zircon ages between 2500-2550 Myr with 2700-3500 Myr ages obtained on detrital or xenocrystal zircons in some samples (Wan et al., 2018). Geothermometry of metasediments suggests that temperatures reached 500-600°C. In general, the grade of metamorphism increases from greenschist facies in the southwest of the area to amphibolite facies in the northeast and east. There is evidence for retrogression of amphibolites to chlorite schists in East Anshan, where the metamorphic grade of BIF is greenschist facies. However, abundant grunerite in our samples supports an amphibolite facies. Textural evidence from schists with garnet and biotite porphyroblasts suggests more than one phase of metamorphism and deformation (Zhai et al., 1990).

Wutai – Baizhiyan Formation, Wutaishan greenstone belt

The Wutaishan greenstone belt in Shanxi province, China has been structurally divided into lower, middle, and upper subgroups (Kusky and Li, 2003; Tian, 1991). The Baizhiyan fm sits in the middle group (Polat et al., 2005). It has been proposed the BIF and associated lithologies were deposited in a closing arc basin, which were juxtaposed by an arc-continent collision at ca. 2500 Myr (Polat et al., 2005). The timing of the orogenic event that resulted in collision of the Western and Eastern continental blocks and deformation of the Wutaishan belt is contentious. The collision was suggested to occur at ca. 1800 Myr (Zhao et al., 2005). However, it was argued that the Wutai arc and Eastern continental block collided between 2550 and 2500 Myr (Kusky and Li, 2003). The belt is folded into a syncline with greenschist facies in the centre grading into amphibolite facies at the margins (Polat et al., 2005).

Brockman iron formation - Dales Gorge member, Hamersley supergroup

The Dales Gorge Member is the lowermost unit of the Brockman Iron Formation in the Hamersley Supergroup, north-western Australia. On the basis of U–Pb ages from zircons extracted from Tuffaceous bands, a depositional age between 2494 and 2464 Myr has been proposed for the dales gorge member (Trendall et al., 2004). Oxygen isotopes of co-existing chert and magnetite along with observable mineralogies suggest the BIF did not exceed lower greenschist facies (Ewers and Morris, 1981; Kaufman et al., 1990).

Biwabik formation, Animikie group

The Biwabik fm. from North America has an age constrained by U-Pb dating from associated volcanic beds bounding the formation, yielding minimum and maximum ages of 1874±9 Myr (Schneider et al., 2002), 1878 ± 1.3 Myr (Fralick et al., 2002) and 1890 ± 10 Myr (Rasmussen et al., 2012). The Biwabik fm. underwent contact metamorphism at ca. 1090 Myr (Paces and Miller, 1993) by intrusion of the Duluth Gabbro Complex, which is observable by mineralogical changes in the iron-formation. Four metamorphic zones may be distinguished within the Biwabik Iron-formation ranging from sub-greenschist to upper amphibolite facies (French, 1968). Sample MF-62-88 represents the highest metamorphic grade of the four zones exhibiting typical high grade BIF mineral assemblages (Klein, 2005) including pyroxene with quartz inclusions.

Pääkkö Formation, Kainuu schist belt

The Pääkkö iron formation is included in the Lower Kaleva successions in eastern Finland within the Kainuu belt (Lahtinen et al., 2010). It is dominantly comprised of amphiboles, quartz and magnetite, with siderite and sulphide rich horizons. The iron formation forms thin 0.5m thick beds (Laajoki and Saikkonen, 1977). The sequence has been metamorphosed to low amphibolite facies (Hölttä and Heilimo, 2017). Based on U-Pb isotopic data from detrital zircons, the Lower Kaleva sedimentation is constrained roughly to 1920-2000 Myr (Kontinen and Hanski, 2015; Lahtinen et al., 2010).

Supplementary Table 1. Energy dispersive spectroscopy elemental compositions of minerals associated with graphitic carbon. Error on measurements 1-4%.

											Elements								
Formation	**Sample**	**Mineral**	**C**	**O**	**F**	**Mg**	**Al**	**Si**	**P**	**S**	**Cl**	**K**	**Ca**	**Cr**	**Mn**	**Fe**	**Co**	**Ni**	**Total**
Akilia	G91-26B	Apatite		33	-	-	-	-	23	-	5	-	39	-	-	-	-	-	100
Akilia	G91-26B	Pyroxene		35	-	5	-	26	-	-	-	-	17	-	-	17	-	-	100
Akilia	G91-26B	Grunerite		35	-	7	-	28	-	-	-	-	-	-	-	30	-	-	100
NSB	PC0814	Apatite		38	-	-	-	-	23		1		38			1			100
NSB	PC0825	Apatite		35	4	-	-	-	23		1		36			1			100
NSB	PC0814	Ferro-hornblende		31	-	1	7	18	-		2	3	8			30			100
NSB	PC-075	Pentlandite	-	-	-	-	-	-	-	33	-	-	-			24	4	39	100
NSB	PC-075	Antigorite		46	-	23	1	22	-		-	-	-			8			100
NSB	PC-075	Calcite	16	44	-	1	-	-	-		-	-	40			-			100
NSB	PC-075	Disseminated magnetite		24			4	1						24	2	45			100
NSB	PC-075	Actinolite	-	42	-	13	3	29	-	-	-	-	10	-	-	2	-	-	100
NSB	PC0825	Minnesotaite		38	-	2	-	26	-		-	-	-			35			100
NSB	PC0825	Greenalite		35	-	1	-	18	-		1	-	-			45			100
Temagami	TE0704	Apatite		38	4	-	-	-	22		-	-	36			-			100
Anshan	ANS0911	Apatite		36	5	-	-	-	21		-		39			-			100
Anshan	ANS0917	Greenalite		36	-	3	-	18	-		-	-	-			42			100
Anshan	ANS0917	Grunerite		35	-	6	-	26	-		-	-	-			34			100
Brockman	Dgh-1-189‘6’’	Apatite		38	3	-	-	-	20		-		37			1			100
Biwabik	MF-62-88	Hedenbergite		38	-	5	-	23	-		-	-	15			18			100
Biwabik	MF-62-88	Grunerite		38	-	5	-	25	-		-	-	1			31			100
Pääkkö	RPK360-15.4	Apatite		39	-	-	-	-	22		-	-	37			-			100

Supplementary Table 2. Raman spectral parameters and crystallisation temperature estimates (Beyssac et al., 2003) for graphitic carbon in samples from this study. NR – not resolvable.

Samples	Carbon type	G-band position	G-band FWHM	D-band posistion	D-band FWHM	2D-band position	2D-band FWHM	D-band area	G+D2 band area	D/G intensity	2D/ G intensity	Temp estimate Beyssac ±50°C	Metamorphic grade
Akilia-G91-26B	Graphite	1583	19.7	NR	NR	2709	56	0	545	0	0.5	641	Granulite (>650°C)
Nuvvuaqittuq-PC0810	Graphite	1583	21.6	1350	33.8	2702	71.7	241	913	0.2	0.3	546	Amphibolite (500-650°C)
Nuvvuaqittuq-PC0810	PCG	1586	26.6	1350	34.2	2692	62.5	1022	537	1.8	0.6	343	Amphibolite (500-650°C)
Nuvvuaqittuq-PC0814	PCG	1583	24.8	1354	37.2	2698	62.5	1605	3205	0.3	0.3	489	Amphibolite (500-650°C)
Nuvvuaqittuq-PC0814	PCG	1588	38.1	1353	41.4	2693	83.6	3894	2381	1.7	0.2	359	Amphibolite (500-650°C)
Nuvvuaqittuq-PC0825	PCG	1577	33	1348	41.9	2686	71.8	16833	15549	1	0.3	404	Amphibolite (500-650°C)
Sandur-BIFs-8	PCG	1593	40.2	1354	44.0	2696	66.1	644	429	1.8	0.50	368	Greenschist (350-500°C)
Sandur-BIFs-8	Graphite	1590	37.2	1357	46.3	2700	67.0	529	598	0.9	0.29	427	Greenschist (350-500°C)
Temagami – TE0704	PCG	1592	43.1	1359	42.9	2703	65.9	1200	681	1.6	0.1	351	Greenschist (350-500°C)
Anshan-ANS0911	Graphite	1582	26.9	1354	36.4	2698	50.2	516	1020	0.4	0.5	488	Amphibolite (500-650°C)
Anshan-ANS0911	PCG	1591	56.6	1353	43.9	2697	81.1	3271	2152	1.6	0.2	367	Amphibolite (500-650°C)
Wutai-WUT1502	Graphite	1566	30.9	1343	69.2	2675	79.1	802	2721	0.1	0.1	537	Greenschist (350-500°C)
Wutai-WUT1502	PCG	1590	67.8	1353	63.9	2696	106.3	4613	3182	1.4	0.4	372	Greenschist (350-500°C)
Dales gorge-DGH-1-198'6	Kerogen	1601	50.4	1348	68.7	NR	NR	6917	3464	1.5	NR	338	Lower greenschist (350-400°C)
Biwabik-MF-62-88	Graphite	1585	27.8	1354	45.1	2700	57.5	549	1485	0.1	0.3	518	Granulite (>650°C)
Pääkkö – RPK360-15.4	Graphite	1578	21.9	1351	39.9	2701	71.2	2565	6812	0.2	0.1	517	Low amphibolite (450-550°C)

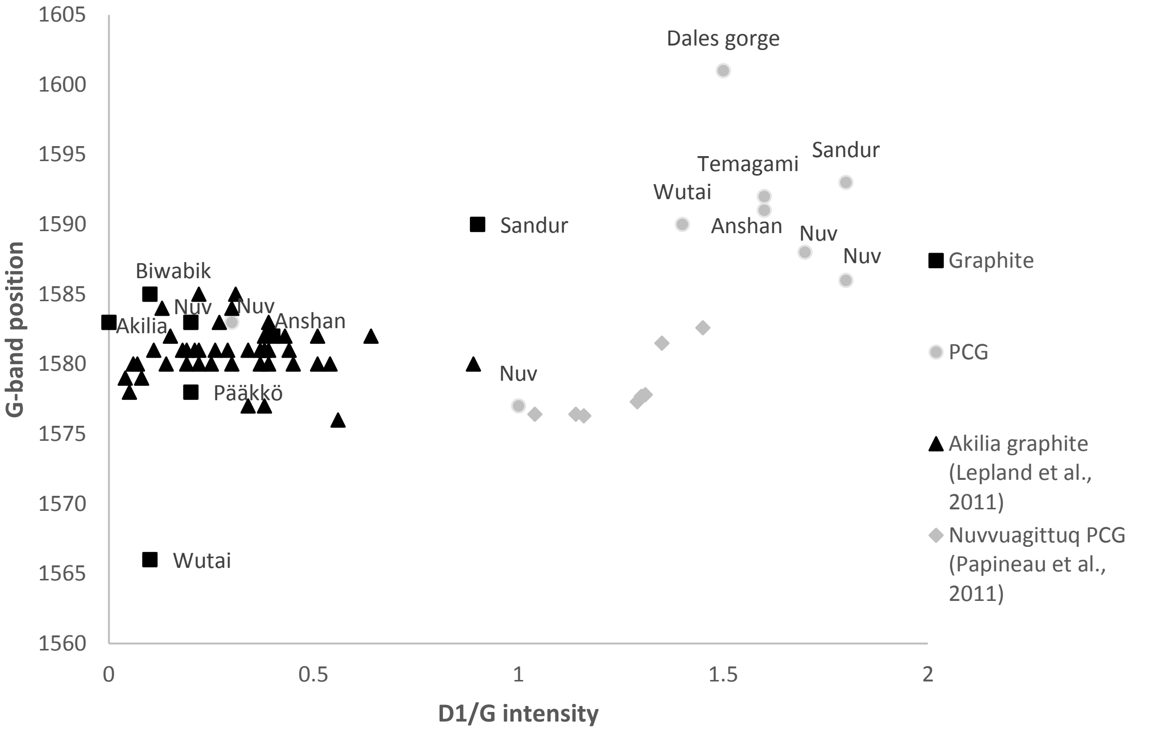

Supplementary Figure 1. Selected Raman parameters for the various types of graphitic carbon in the banded iron formations presented here, compared with other graphitic Raman parameters from other studies. Note poorly crystalline graphite (PCG) generally have D1/ G peak intensities higher than 1, and crystalline graphite less than 1. Also, PCG on average tends to have higher G-band positions than crystalline graphite.

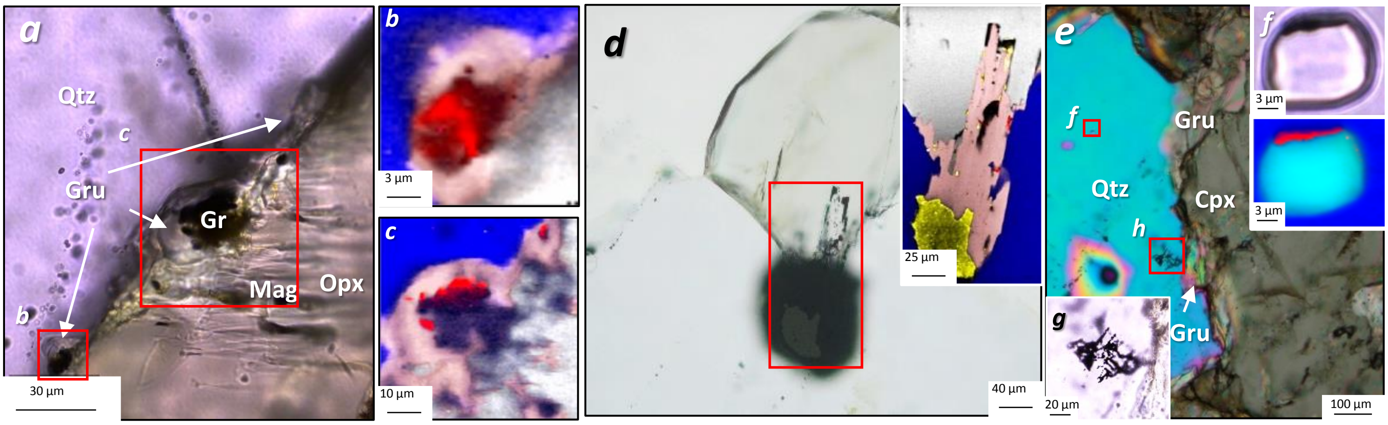

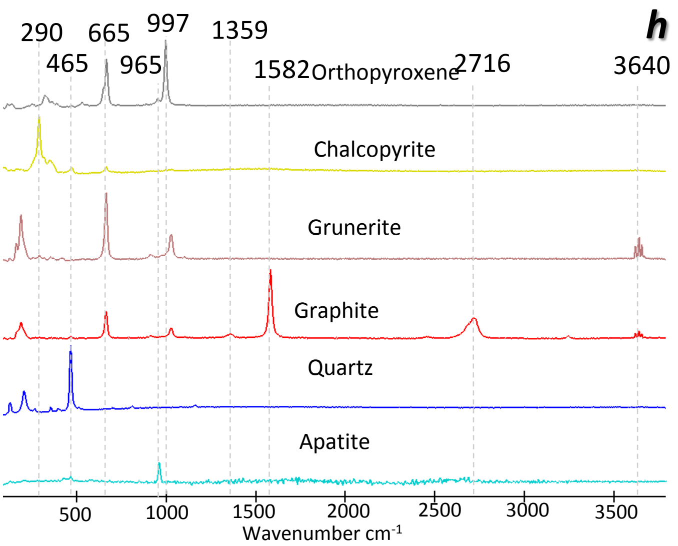

Supplementary figure 2. Graphite associations in the Akilia quartz-pyroxene rock. a) PPL image of orthopyroxene with retrograde grunerite rims including graphitic carbon. b-c) Raman maps showing inclusions of graphite in retrograde grunerite rims on orthopyroxene. d) PPL image of grunerite and chalcopyrite with clinopyroxene. Inset is Raman map of the boxed area showing graphite occurs in retrograde grunerite with chalcopyrite. e) CP image of apatite associate with graphitic carbon in the Akilia BIF. f) PPL image of apatite crystal with graphitic carbon coating with Raman map apatite with graphite coating. g) PPL image of branching graphite extending from a grunerite rim on pyroxene. h) Representative Raman spectra for this figure.

Supplementary table 3 Comparative table of organic matter reported from Precambrian BIF (ordered by decreasing metamorphic grades) along with key characteristics and interpreted origins.

Banded iron formation + Age	Metamorphic grade	Organic matter crystallinity	Summary of key observations	Interpretation of the origin of graphitic carbons*	References
Akilia **Ca. 3, 830 Myr**	**Granulite**	Graphite	Graphite is isotopically light. Graphite occurs with retrograde grunerite. Some graphite has curled structures. As well as with apatite±calcite±chalcopyrite±pentlandite±pyrrhotite±magnetite. C-H bonds in apatite have been reported, although not clearly syngenetic. Graphite occurs nearby fluid inclusions of CO_2+CH_4. Graphite contains CHNOPS elements.	The presence of crystalline graphite and curled graphite structures suggest formation during prograde metamorphism at the granulite facies. The co-occurrence with fluid inclusions indicates some of the graphite+apatite occurrences are fluid-deposited. The isotopic and elemental composition of graphite are consistent with biomass, although fluid-deposited graphite could have sourced non-biological carbon. The null hypothesis is not fully rejected.	(Mojzsis et al., 1996; Nutman and Friend, 2006 ; McKeegan et al., 2007; Papineau et al., 2010a; Papineau et al., 2010b; Lepland et al., 2005 ; 2011) ;
Biwabik **Ca. 1, 880 Myr**	**Granulite**	Graphite	Graphite is isotopically light. Graphite occurs with retrograde grunerite and calcite. In other granular iron formation from the Biwabik group, apatite occurs with carbonate and kerogen in greenschist facies granular and stromatolitic jasper. These jaspers also contain rosettes and microfossils.	Isotopic composition of graphite is consistent with metamorphosed biomass, and also consistent with observed microbialites in this formation. Graphite in retrograde grunerite suggests some graphite may have formed during fluid deposition during retrogression.	This work; see also Papineau et al., 2017; Dodd et al., 2018 Shapiro and Konhauser, 2015; Laberge, 1973, Lougheed, 1983
Vichadero **Ca. 2, 200 Myr**	**Granulite**	Graphite	Graphite is isotopically light, and contains CHNOPS elements. Graphite occurs along apatite margins with haematite and carbonate, and nearby fluid inclusions of CO_2+CH4. Apatite grains form dense layers.	Graphite crystallinity consistent with prograde metamorphism. The isotopic and elemental composition of the graphite are consistent with biomass. Association of apatite and graphite with fluid inclusions points to the fluid-deposition of some graphite.	(Papineau et al., 2010b)
Saglek **Ca. 3, 780-3, 920 Myr**	**Upper amphibolite/ granulite**	Graphite	Graphite is isotopically light and occurs within and along apatite margins. Apatite grains 10s to 100s of microns in size.	Graphite crystallinity consistent with prograde metamorphism. The isotopic compositions of graphite in associated sediments from the belt are consistent with biomass, and the possible presence of stromatolites. However, the null hypothesis is not fully rejected for the graphite occurring with apatite.	This work; (Komiya et al., 2015; Tashiro et al., 2017; Morino et al., 2017)
Nuvvuagittuq **Ca. 3, 770-4,280 Myr**	**Upper amphibolite**	Graphite + PCG	Bulk rock organic carbon is isotopically light. Graphite occurs with apatite, 13C-depleted carbonate, or as inclusions in pyroxene. Graphite also occurs with carbonate and apatite associated with bundles of haematite filaments, rosettes and granules. PCG occurs with retrograde minerals, including cronstedtite, poly-sulphides, minnesotaite, greenalite, hornblende and apatite.	During graphitisation, carbon species devolatilised into fluids and later precipitated as PCG with apatite nearby, during retrograde metamorphism. The isotopic composition of graphite and its association with apatite and carbonate in sedimentological structures and microfossils is consistent with metamorphosed biomass, and the null hypothesis can be rejected. However, the null hypothesis is not fully rejected for fluid-deposited PCG.	This work; (Papineau et al., 2011; Dodd et al., 2017)
Isua **Ca. 3, 700 Myr**	**Amphibolite**	Graphite	Graphite is isotopically light and occurs with apatite and carbonate	Isotopic composition of graphite and association with apatite are not inconsistent with metamorphosed biomass. However the null hypothesis has not yet been entirely rejected.	(Mojzsis et al., 1996; Van Zuilen et al., 2002; Lepland et al., 2002)
Michigamme **Ca. 1, 850 Myr**	**Amphibolite**	Graphite	Graphite is isotopically light, and contains CHNOPS elements. Graphite occurs within dolomite and apatite.	Graphite crystallinity, mineral associations, and elemental composition of the graphite suggest graphite formed from metamorphosed biomass. This is consistent with the presence of microbialites in this formation.	(Papineau et al., 2010b)
Anshan **Ca. 2, 550 Myr**	**Amphibolite**	Graphite + PCG	Bulk rock organic carbon is isotopically light. Graphite occurs within prograde grunerite and with apatite. PCG occurs with retrograde greenalite, as well as apatite	Isotopic composition of graphite and association with apatite is consistent with it having formed from metamorphosed biomass. During graphitisation, carbon species devolatilised into fluids and later precipitated as PCG nearby	This work
Pääkkö **Ca. 2, 000 Myr**	**Amphibolite**	Graphite	Graphite is isotopically light and occurs within prograde grunerite, with apatite, magnetite and feldspar	Isotopic composition of graphite and its occurrence within prograde grunerite suggest the graphite is formed from syngenetic organic matter, and likely biomass.	This work
Wutai – Baizhiyan fm. **Ca. 2,500 Myr**	**Upper greenschist**	Graphite + PCG	Bulk rock organic carbon is isotopically light. Graphite and PCG occur within ^{13}C-depleted ankerite and close (microns) proximity to apatite	Isotopic composition of graphite and association with 13C-depleted ankerite are consistent with it having formed from metamorphosed biomass. During graphitisation carbon species were volatilised and later precipitated as PCG	This work
Sandur **Ca. 2, 700 Myr**	**Greenschist**	Graphite + kerogen	Bulk rock organic carbon is isotopically light. Graphite occurs along quartz grain boundaries or co-occurring with kerogen. Both graphite and kerogen are associated with apatite, pyrite and ^{13}C-depleted siderite.	Graphite may have formed during templated growth on quartz grain boundaries. Isotopic composition of kerogen and association with apatite are consistent with it having formed from metamorphosed biomass.	This work
Temagami **Ca. 2, 700 Myr**	**Greenschist**	Kerogen	Kerogen is isotopically light and occurs within apatite and ^{13}C-depleted ankerite.	Isotopic composition of kerogen and association with apatite and ^{13}C-depleted ankerite are consistent with formation from metamorphosed biomass.	This work
Dales Gorge **Ca. 2,500 Myr**	**Lower greenschist**	Kerogen	Kerogen is isotopically light and occurs within apatite and ^{13}C-depleted siderite. Ferrous acetate found associated with apatite.	Characteristics are consistent with formation from metamorphosed biomass, which is also consistent with interbedded black shales that are rich in organic matter of biological origin.	This work; (Mojzsis et al., 1996; Li et al., 2011)

* The null hypothesis tests are mentioned only for Eoarchean metasedimentary rocks, as there is little debate about the prevalence of life on Earth since the Neoarchean.

References

André, L., Cardinal, D., Alleman, L. Y., and Moorbath, S., 2006, Silicon isotopes in ~3.8 Ga West Greenland rocks as clues to the Eoarchaean supracrustal Si cycle: Earth and Planetary Science Letters, v. 245, no. 1, p. 162-173.
Boily, M., Leclair, A., Maurice, C., Bédard, J. H., and David, J., 2009, Paleo- to Mesoarchean basement recycling and terrane definition in the Northeastern Superior Province, Québec, Canada: Precambrian Research, v. 168, no. 1-2, p. 23-44.
Bolhar, R., Kamber, B. S., Moorbath, S., Fedo, C. M., and Whitehouse, M. J., 2004, Characterisation of early Archaean chemical sediments by trace element signatures: Earth and Planetary Science Letters, v. 222, no. 1, p. 43-60.
Bowins, R. J., and Heaman, L. M., 1991, Age and timing of igneous activity in the Temagami greenstone belt, Ontario: a preliminary report: Canadian Journal of Earth Sciences, v. 28, no. 11, p. 1873-1876.
Cates, N. L., and Mojzsis, S. J., 2007, Pre-3750 Ma supracrustal rocks from the Nuvvuagittuq supracrustal belt, northern Québec: Earth and Planetary Science Letters, v. 255, no. 1-2, p. 9-21.
-, 2009, Metamorphic zircon, trace elements and Neoarchean metamorphism in the ca. 3.75 Ga Nuvvuagittuq supracrustal belt, Québec (Canada): Chemical Geology, v. 261, no. 1-2, p. 99-114.
Cates, N. L., Ziegler, K., Schmitt, A. K., and Mojzsis, S. J., 2013, Reduced, reused and recycled: Detrital zircons define a Maximum age for the Eoarchean (ca. 3750–3780Ma) Nuvvuagittuq Supracrustal Belt, Québec (Canada): Earth and Planetary Science Letters, v. 362, p. 283-293.
Collerson, K. D., and Bridgwater, D., 1979, Chapter 7 - Metamorphic Development of Early Archean Tonalitic and Trondhjemitic Gneisses: Saglek Area, Labrador, in Barker, F., ed., Developments in Petrology, Volume 6, Elsevier, p. 205-273.
Dai, Y.P., Zhang, L.C., Zhu, M.T, Wang, C.L., Liu, L., 2013. Chentaigou BIF-type iron deposit, Anshan area associated with Archean crustal growth: Constraints from zircon U-Pb dating and Hf isotope. Acta Petrologica Sinica, 29(7): 2537-2550
Darling, J. R., Moser, D. E., Heaman, L. M., Davis, W. J., O'Neil, J., and Carlson, R., 2013, Eoarchean to Neoarchean evolution of the Nuvvuagittuq Supracrustal belt: New insights from U-Pb zircon geochronology: American Journal of Science, v. 313, no. 9, p. 844-876.
Dauphas, N., van Zuilen, M., Wadhwa, M., Davis, A. M., Marty, B., and Janney, P. E., 2004, Clues from Fe isotope variations on the origin of early Archean BIFs from Greenland: Science, v. 306, no. 5704, p. 2077-2080.
David, J., Godin, L., Stevenson, R., O'Neil, J., and Francis, D., 2009, U-Pb ages (3.8-2.7 Ga) and Nd isotope data from the newly identified Eoarchean Nuvvuagittuq supracrustal belt, Superior Craton, Canada: Geological Society of America Bulletin, v. 121, no. 1-2, p. 150-163.
Ewers, W. E., and Morris, R. C., 1981, Studies of the Dales Gorge Member of the Brockman Iron Formation, Western Australia: Economic Geology, v. 76, no. 7, p. 1929-1953.
Fedo, C. M., and Whitehouse, M. J., 2002, Metasomatic origin of quartz-pyroxene rock Akilia Greenland and implications for Earths earliest life: Science v. 296, p. 1448-1452.
Fralick, P., Davis, D. W., and Kissin, S. A., 2002, The age of the Gunflint Formation, Ontario, Canada: single zircon U–Pb age determinations from reworked volcanic ash: Canadian Journal of Earth Sciences, v. 39, p. 1085-1091.
French, B. M., 1964, Graphitization of Organic Material in a Progressively Metamorphosed Precambrian Iron Formation: Science, v. 146, no. 3646, p. 917-918.
-, 1968, Progressive Contact Metamorphism of the Biwabik Iron-formation, Mesabi Range, Minnesota: Minnesota Geological Survey.
Guitreau, M., Blichert-Toft, J., Mojzsis, S. J., Roth, A. S. G., and Bourdon, B., 2013, A legacy of Hadean silicate differentiation inferred from Hf isotopes in Eoarchean rocks of the Nuvvuagittuq supracrustal belt (Québec, Canada): Earth and Planetary Science Letters, v. 362, p. 171-181.
Hölttä, P., and Heilimo, E., 2017, Metamorphic map of Finland *in* Nironen, M., ed., Bedrock of Finland at the scale 1:1 000 000 - Major stratigraphic units, metamorphism and tectonic evolution, p. 77-128.
Kaufman, A. J., Hayes, J. M., and Klein, C., 1990, Primary and diagenetic controls of isotopic compositions of iron-formation carbonates: Geochimica et Cosmochimica Acta, v. 54, no. 12, p. 3461-3473.
Ishikawa, A., Suzuki, K., Collerson, K. D., Liu, J., Pearson, D. G., and Komiya, T., 2017, Rhenium-osmium isotopes and highly siderophile elements in ultramafic rocks from the Eoarchean Saglek Block, northern Labrador, Canada: implications for Archean mantle evolution: Geochimica et Cosmochimica Acta, v. 216, p. 286-311.
Kinny, P. D., 1986, 3820 Ma zircons from a tonalitic Armîsoq gneiss in the Godthåb district of Southern West Greenland: Earth and Planetary Science Letters, v. 79, no. 3, p. 337-347.
Klein, C., 2005, Some Precambrian banded iron-formations (BIFs) from around the world: Their age, geologic setting, mineralogy, metamorphism, geochemistry, and origins: American Mineralogist, v. 90, no. 10, p. 1473-1499.
Komiya, T., Yamamoto, S., Aoki, S., Sawaki, Y., Ishikawa, A., Tashiro, T., Koshida, K., Shimojo, M., Aoki, K., and Collerson, K. D., 2015, Geology of the Eoarchean, >3.95Ga, Nulliak supracrustal rocks in the Saglek Block, northern Labrador, Canada: The oldest geological evidence for plate tectonics: Tectonophysics, v. 662, p. 40-66.
Komiya, T., Yamamoto, S., Aoki, S., Koshida, K., Shimojo, M., Sawaki, Y., Aoki, K., Sakata, S., Yokoyama, T. D., Maki, K., Ishikawa, A., Hirata, T., and Collerson, K. D., 2017, A prolonged granitoid formation in Saglek Block, Labrador: Zonal growth and crustal reworking of continental crust in the Eoarchean: Geoscience Frontiers, v. 8, no. 2, p. 355-385.
Kontinen, A., and Hanski, E., 2015, The Talvivaara black shale-hosted Ni-Zn-Cu-Co deposit in eastern Finland., *in* Maier, W. D. O. B., H: Lahtinen, R, ed., Mineral Deposits of Finland, Elsevier, p. 557-607.
Kusiak, M. A., Dunkley, D. J., Whitehouse, M. J., Wilde, S. A., Sałacińska, A., Konečný, P., Szopa, K., Gawęda, A., and Chew, D., 2018, Peak to post-peak thermal history of the Saglek Block of Labrador: A multiphase and multi-instrumental approach to geochronology: Chemical Geology, v. 484, p. 210-223.
Kusky, T. M., and Li, J., 2003, Paleoproterozoic tectonic evolution of the North China Craton: Journal of Asian Earth Sciences, v. 22, no. 4, p. 383-397.

Laajoki, K., and Saikkonen, R., 1977, On the geology and geochemistry of the Precambrian iron forMations in Väyrylänkylä, South Puolanka area, Finland Bull. Geol. Soc. Finland, v. 292.
Lahtinen, R., Huhma, H., Kontinen, A., Kohonen, J., and Sorjonen-Ward, P., 2010, New constraints for the source characteristics, deposition and age of the 2.1–1.9Ga metasedimentary cover at the western margin of the Karelian Province: Precambrian Research, v. 176, no. 1, p. 77-93.
Manikyamba, C., Balaram, V., and Naqvi, S. M., 1993, Geochemical signatures of polygenetic origin of a banded iron formation (BIF) of the Archaean Sandur greenstone belt (schist belt) Karnataka nucleus, India: Precambrian Research, v. 61, no. 1, p. 137-164.
Manikyamba, C., and Naqvi, S. M., 1996, Evidence of Archaean crustal shortening from deformed pillow lavas: An example from Sandur greenstone belt, Dharwar craton: Current Science, v. 71, no. 6, p. 476-479.
Manning, C. E., Mojzsis, S. J., and Harrison, M., 2006, Geology, Age and Origin of Supracrustal Rocks at Akilia, West Greenland: American Journal of Science, v. 306, no. 5, p. 303-366.
McGregor, V. R., and Mason, B., 1977, Petrogenesis and geochemistry of metabasaltic and metasedimentary enclaves in the Amıtsoq gneisses, West Greenland: American Mineralogist, v. 62, p. 887-904.
Morino, P., Caro, G., Reisberg, L., and Schumacher, A., 2017, Chemical stratification in the post-magma ocean Earth inferred from coupled 146,147Sm–142,143Nd systematics in ultramafic rocks of the Saglek block (3.25–3.9 Ga; northern Labrador, Canada): Earth and Planetary Science Letters, v. 463, p. 136-150.
Mukhopadhyay, D., and Matin, A., 1993, The structural anatomy of the Sandur schist belt—a greenstone belt in the Dharwar craton of South India: Journal of Structural Geology, v. 15, no. 3, p. 309-322.
Naqvi, S. M., Manikyamba, C., Gnaneshwar Rao, T., Subba Rao, D. V., Ram Mohan, M., and Srinivasa Sarma, D., 2002, Geochemical and Isotopic Constraints of Neoarchaean Fossil Plume for Evolution of Volcanic Rocks of Sandur Greenstone Belt, India, 2002.
Nutman, A. P., Chadwick, B., Krishna Rao, B., and Vasudev, V. N., 1996, SHRIMP U/Pb Zircon Ages of Acid Volcanic Rocks in the Chitradurga and Sandur Groups, and Granites Adjacent to the Sandur Schist Belt, Karnataka, 1996.
Nutman, A. P., McGregor, V. R., Shiraishi, K., Friend, C. R. L., Bennett, V. C., and Kinny, P. D., 2002, ⩾3850 Ma BIF and Mafic inclusions in the early Archaean Itsaq Gneiss Complex around Akilia, southern West Greenland? The difficulties of precise dating of zircon-free protoliths in migmatites: Precambrian Research, v. 117, no. 3, p. 185-224.
Nutman, A. P., Mojzsis, S. J., and Friend, C. R. L., 1997, Recognition of ≥3850 Ma water-lain sediments in West Greenland and their significance for the early Archaean Earth: Geochimica et Cosmochimica Acta, v. 61, no. 12, p. 2475-2484.
O'Neil, J., Maurice, C., Stevenson, R. K., Larocque, J., Cloquet, C., David, J., and Francis, D., 2007, The Geology of the 3.8 Ga Nuvvuagittuq (Porpoise Cove) Greenstone Belt, Northeastern Superior Province, Canada, *in* Kranendonk, M. J. v., Smithies, R. H., and Bennett, V. C., eds., Earth's Oldest Rocks, Volume 15, Elsevier B.V, p. 219-250.
O'Neil, J., Carlson, R. W., Francis, D., and Stevenson, R. K., 2008, Neodymium-142 Evidence for Hadean Mafic Crust: Science, v. 321, p. 1828-1831.
O'Neil, J., Carlson, R. W., Paquette, J.-L., and Francis, D., 2012, Formation age and metamorphic history of the Nuvvuagittuq Greenstone Belt: Precambrian Research, v. 220-221, p. 23-44.
O'Neil J., Carlson, R.W., Papineau, D., Levine, E.Y. and Francis, D. (2019). Chapter 16 - The Nuvvuagittuq Greenstone Belt: A Glimpse of Earth's Earliest Crust. Earth's Oldest Rocks (Second Edition). M. J. Van Kranendonk, V. C. Bennett and J. E. Hoffmann, Elsevier: 349-374.
Paces, J. B., and Miller, J. D., 1993, Precise U-Pb ages of Duluth Complex and related mafic intrusions, northeastern Minnesota: Geochronological insights to physical, petrogenetic, paleomagnetic, and tectonomagmatic processes associated with the 1.1 Ga Midcontinent Rift System: Journal of Geophysical Research: Solid Earth, v. 98, no. B8, p. 13997-14013.
Polat, A., and Frei, R., 2005, The origin of early Archean banded iron formations and of continental crust, Isua, southern West Greenland: Precambrian Research, v. 138, no. 1-2, p. 151-175.
Polat, A., Kusky, T., Li, J., Fryer, B., Kerrich, R., and Patrick, K., 2005, Geochemistry of Neoarchean (ca. 2.55–2.50 Ga) volcanic and ophiolitic rocks in the Wutaishan greenstone belt, central orogenic belt, North China craton: Implications for geodynamic setting and continental growth: Geological Society of America Bulletin, v. 117, no. 11, p. 1387.
Rasmussen, B., Fletcher, I. R., Bekker, A., Muhling, J. R., Gregory, C. J., and Thorne, A. M., 2012, Deposition of 1.88-billion-year-old iron formations as a consequence of rapid crustal growth: Nature, v. 484, no. 7395, p. 498-501.
Roth, A. S. G., Bourdon, B., Mojzsis, S. J., Touboul, M., Sprung, P., Guitreau, M., and Blichert-Toft, J., 2013, Inherited 142Nd anomalies in Eoarchean protoliths: Earth and Planetary Science Letters, v. 361, p. 50-57.
Schiøtte, L., Bridgwater, D., Collerson, K. D., Nutman, A. P., and Ryan, A. B., 1986, Chemical and isotopic effects of late Archaean high-grade metamorphism and granite injection on early Archaean gneisses, Saglek-Hebron, northern Labrador: Geological Society, London, Special Publications, v. 24, no. 1, p. 261-273.
Schneider, D. A., Bickford, M. E., Cannon, W. F., Schulz, K. J., and Hamilton, M. A., 2002, Age of volcanic rocks and syndepositional iron formations, Marquette Range Supergroup: implications for the tectonic setting of Paleoproterozoic iron formations of the Lake Superior region: Canadian Journal of Earth Sciences, v. 39, no. 6, p. 999-1012.
Shimojo, M., Yamamoto, S., Sakata, S., Yokoyama, T. D., Maki, K., Sawaki, Y., Ishikawa, A., Aoki, K., Aoki, S., Koshida, K., Tashiro, T., Hirata, T., Collerson, K. D., and Komiya, T., 2016, Occurrence and geochronology of the Eoarchean, ∼3.9Ga, Iqaluk Gneiss in the Saglek Block, northern Labrador, Canada: Evidence for the oldest supracrustal rocks in the world: Precambrian Research, v. 278, p. 218-243.
Tian, Y. Q., 1991, Geology and mineralization of the Wutai-Hengshan greenstone belt: Shanxi Science and Technology Press, Taiwan, p. 137-152.
Trendall, A. F., 2002, The significance of iron-formation in the Precambrian stratigraphic record, *in* AlterMann, W., and Corcoran, P. L., eds., Precambrian Sedimentary Environments: A Modern Approach to Ancient Depositional Systems, International Association of Sedimentologists.

Wan, Y.S., Liu, D.Y., Xie, H.Q., Kröner, A., Ren, P., Liu, S.J., Xie, S.W., Dong, C.Y., Ma, M.Z., 2016. Formation ages and environments of Early Precambrian banded iron formation in the North China Craton. In: Zhai, M.G. (Ed.) Main tectonic events and metallogeny of the North China Craton. Springer, 65-83.
Wan, Y.S., Dong, C.Y., Xie, H.Q., Xie, S.W., Liu, S.J., Bai, W.Q., Ma, M.Z., Liu, D.Y., 2017. Formation age of the BIF-bearing Anshan Group supracrustal rocks: New evidence from SHRIMP U-Pb zircon dating. Earth Science.
Wendt, J. I., and Collerson, K. D., 1999, Early Archæan U/Pb fractionation and timing of late Archæan high-grade metamorphism in the Saglek–Hebron segment of the North Atlantic Craton: Precambrian Research, v. 93, no. 4, p. 281-297.
Whitehouse, M. J., and Kamber, B. S., 2005, Assigning Dates to Thin Gneissic Veins in High-Grade Metamorphic Terranes: A Cautionary Tale from Akilia, Southwest Greenland: Journal of Petrology, v. 46, no. 2, p. 291-318.
Zhai, M., Windley, B. F., and Sills, J. D., 1990, Archaean gneisses, amphibolites and banded iron-formations from the Anshan area of Liaoning Province, NE China: Their geochemistry, metamorphism and petrogenesis: Precambrian Research, v. 46, no. 3, p. 195-216.
Zhao, G., Sun, M., Wilde, S. A., and Sanzhong, L., 2005, Late Archean to Paleoproterozoic evolution of the North China Craton: key issues revisited: Precambrian Research, v. 136, no. 2, p. 177-202.
Zhao, G., Wilde, S. A., Cawood, P. A., and Sun, M., 2002, SHRIMP U–Pb zircon ages of the Fuping Complex: Implications for Late Archean to Paleoproterozoic accretion and assembly of the North China Craton: American Journal of Science, v. 302, no. 3, p. 191-226.